



Supplementary Materials for  
**Entangling microwaves with light**

R. Sahu *et al.*

Corresponding authors: R. Sahu, rsahu@ist.ac.at; L. Qiu, liu.qiu@ist.ac.at; J. M. Fink, jfink@ist.ac.at

*Science* **380**, 718 (2023)  
DOI: 10.1126/science.adg3812

**The PDF file includes:**

Supplementary Text  
Figs. S1 to S15  
Tables S1 and S2  
References

## CONTENTS

	Page
I. Theory	3
A Covariance Matrix from Input-Output Theory . . . . .	3
1 Quantum Langevin Equations . . . . .	3
2 Input-Output-Theory . . . . .	4
3 Covariance Matrix of Filtered Output Fields . . . . .	6
B Heterodyne Detection, Added Noise and Filtering . . . . .	7
1 Heterodyne Measurement . . . . .	7
2 Realistic Measurements: Added Noise and Gain . . . . .	8
3 Covariance Matrix from Realistic Heterodyne Measurements . . . . .	9
C Entanglement Detection . . . . .	10
1 Duan Criterion . . . . .	10
2 Logarithmic Negativity, Purity and Effective Squeezing . . . . .	11
II. Experimental Setup	11
III. Setup Characterization and Calibration	11
A Microwave Added Noise Calibration . . . . .	13
B Optical Added Noise . . . . .	14
IV. Data Treatment	15
A Time-domain Analysis . . . . .	15
B Pulse Post-selection . . . . .	17
C Frequency Domain Analysis . . . . .	17
D Joint-quadrature Correlations . . . . .	19
V. Quadrature Histogram Raw Data	20
VI. Non-classical Correlations with 600 ns Long Optical Pump Pulses	21
VII. Error Analysis	21
A Statistical Error . . . . .	22
B Systematic Error . . . . .	23
VIII. Entanglement Figures of Merit	23
IX. Future Applications	24

---

Introduced in Main Text	
$\hat{a}_e$	microwave mode (annihilation operator)
$m_e$	microwave mode azimuthal number, $m_e = 1$
$\omega_e$	microwave cavity frequency
$\kappa_e, \kappa_{e,\text{eff}}, \kappa_{e,\text{in}}, \kappa_{e,0}$	microwave total loss, effective total loss, waveguide coupling and intrinsic loss rates
$\bar{n}_{e,\text{int}}, \bar{n}_{e,\text{wg}}$	microwave intrinsic and waveguide bath occupancy
$N_{e,\text{add}}$	added noise in the microwave detection
$\hat{a}_o, \hat{a}_p, \hat{a}_t, \hat{a}_{\text{tm}}$	optical Stokes, pump, anti-Stokes, and transverse-magnetic mode (annihilation operator)
$\hat{a}_{e/o,\text{out}}$	microwave and optical output field from the device
$m_p$	optical pump mode azimuthal number, $m_p \sim 20000$
$\kappa_o$	optical total loss rate
$N_{o,\text{add}}$	added noise in the optical detection
$\bar{n}_p$	mean photon number of the optical pump mode
$g_0$	electro-optical vacuum coupling rate
$g$	photon enhanced electro-optical coupling rate ( $g = \sqrt{\bar{n}_p} g_0$ )
$C$	cooperativity ( $C = 4g^2/\kappa_e\kappa_o$ )
$X_e, P_e$	quadratures of the microwave output field
$X_o, P_o$	quadratures of the optical Stokes output field
$V$	covariance matrix of the bipartite Gaussian state, $V_{ij} = \langle \Delta u_i \Delta u_j + \Delta u_j \Delta u_i \rangle / 2$ , where $\Delta u_i = u_i - \langle u_i \rangle$ and $u \in \{X_e, P_e, X_o, P_o\}$ .
$N_{ii,\text{add}}$	added noise in the quadrature variances measurements, $N_{11,\text{add}} = N_{22,\text{add}} = N_{e,\text{add}}$ , $N_{33,\text{add}} = N_{44,\text{add}} = N_{o,\text{add}}$
$V_{ii,\text{meas}}$	diagonal covariance matrix elements from the calibrated measurement record, $V_{ii} = V_{ii,\text{meas}} - N_{ii,\text{add}}$
$V_{11}, V_{22}, \bar{V}_{11}$	quadrature variances of the microwave output field, $\bar{V}_{11} = \frac{V_{11}+V_{22}}{2}$
$V_{33}, V_{44}, \bar{V}_{33}$	quadrature variances of the optical Stokes output field, $\bar{V}_{33} = \frac{V_{33}+V_{44}}{2}$
$V_{13}, V_{24}, \bar{V}_{13}$	cross-correlation between microwave and optical quadratures, $\bar{V}_{13} = \frac{V_{13}-V_{24}}{2}$
$\Delta_{\text{EPR}}^\pm$	squeezed and anti-squeezed joint quadrature variance between microwave and optical output field, $\Delta_{\text{EPR}}^\pm = \bar{V}_{11} + \bar{V}_{33} \mp \bar{V}_{13}$
Introduced in Supplementary Material	
$J$	coupling rate between the optical anti-Stokes mode and TM mode
$\hat{a}_{e/o,\text{in}}$	input field (noise) operator for the microwave and optical mode
$\hat{a}_{e/o,0}$	noise operator for the microwave and optical intrinsic loss
$\eta_j$	external cavity coupling efficiency of individual mode, $j \in (e, o, p, t)$
$\mathcal{G}(\omega)$	spectral filter of the output field
$\hat{A}(\Omega)$	Fourier transform of operator $\hat{A}(t)$ , $\hat{A}(\Omega) = \int dt e^{i\Omega t} \hat{A}(t)$ , $\hat{A}^\dagger(\Omega) = \int dt \hat{A}^\dagger(t) e^{i\Omega t} = [\hat{A}(-\Omega)]^\dagger$
$\hat{X}(\omega_n)$	$X$ quadrature of the output spectral mode, $\hat{X}(\omega_n) = \frac{1}{\sqrt{2}} \int_{-\infty}^{\infty} d\omega \mathcal{G}(\omega_n - \omega) \hat{a}_{\text{out}}(\omega) + \text{h.c.}$
$\hat{P}(\omega_n)$	$P$ quadrature of the output spectral mode, $\hat{P}(\omega_n) = \frac{1}{\sqrt{2i}} \int_{-\infty}^{\infty} d\omega \mathcal{G}(\omega_n - \omega) \hat{a}_{\text{out}}(\omega) + \text{h.c.}$
$S_{\hat{A}\hat{B}}(\Omega)$	Two-time correlation of two operators, $S_{\hat{A}\hat{B}}(\Omega) = \frac{1}{\sqrt{2\pi}} \int_{-\infty}^{\infty} \langle \hat{A}(t) \hat{B}(t') \rangle e^{i\Omega t} dt$
$\Delta_{\text{LO}}$	local oscillator and signal frequency difference in heterodyne measurement, $\Delta_{\text{LO}} = \omega_{\text{LO}} - \omega_{\text{sig}}$
$I_{\text{out}}(t), I_{\text{out}}(\omega)$	unitless output field in the equivelant heterodyne detection
$S_{II}(\omega)$	double-sided noise spectrum of the output field in the equivelant heterodyne detection
$G_{\text{det}}(\omega)$	frequency dependent detection gain in the heterodyne detection
$\hat{I}_{X/P,\text{det}}(\omega_n)$	detected output photocurrent quadratures in heterodyne detection, including detection gain
$\hat{I}_{X/P,\text{out}}(\omega_n)$	unitless output field quadratures from $I_{\text{out}}$ including added noise
$\mathcal{D}(\omega)$	covariance matrix of the detected quadratures <i>from the heterodyne measurement record</i>
$V_{\text{meas}}(\omega)$	covariance matrix of the total measured output field quadratures including added noise
$\hat{X}_+(\omega)$	joint quadrature of $\hat{X}_e(\omega)$ and $\hat{X}_o(-\omega)$ , $\hat{X}_+(\omega) = (\hat{X}_e(\omega) + \hat{X}_o(-\omega))/\sqrt{2}$
$\hat{P}_-(\omega)$	joint quadrature of $\hat{P}_e(\omega)$ and $\hat{P}_o(-\omega)$ , $\hat{P}_-(\omega) = (\hat{P}_e(\omega) - \hat{P}_o(-\omega))/\sqrt{2}$
$E_N$	logarithm negativity
$\rho$	state purity

## I. THEORY

### A. Covariance Matrix from Input-Output Theory

#### 1. Quantum Langevin Equations

Our cavity electro-optical (CEO) device consists of a millimeter-sized lithium niobate optical resonator in a 3-D superconducting microwave cavity at mK temperature (24). The Pockels effect in lithium niobate allows for direct coupling between the microwave and optical whispering gallery modes with maximal field overlap. The optical free spectral range (FSR) matches the microwave cavity frequency, with microwave azimuthal mode number  $m_e = 1$ . As shown in Fig. 1 in the main text, resonant three-wave mixing between the microwave mode ( $\hat{a}_e$ ) and three adjacent transverse-electric (TE) optical modes, i.e. Stokes ( $\hat{a}_o$ ), pump ( $\hat{a}_p$ ), and anti-Stokes ( $\hat{a}_t$ ) mode, arises via the cavity enhanced electro-optical interaction (25, 44). In addition, the anti-Stokes mode is coupled to a transverse-magnetic (TM) optical mode ( $\hat{a}_{tm}$ ) of orthogonal polarization and similar frequency at rate of  $J$  (45). This results in a total interaction Hamiltonian,

$$\hat{H}_I/\hbar = g_0(\hat{a}_p^\dagger \hat{a}_e \hat{a}_o + \hat{a}_p^\dagger \hat{a}_e^\dagger \hat{a}_t) + J\hat{a}_t \hat{a}_{tm}^\dagger + h.c., \quad (S1)$$

with  $g_0$  the vacuum electro-optical coupling rate.

For entanglement generation, we drive the pump mode strongly with a short coherent input pulse  $\bar{a}_{p,\text{in}}(t)$  at frequency  $\omega_p$  (24), which results in a time-dependent mean intra-cavity field of the pump mode  $\bar{a}_p(t)$ ,

$$\dot{\bar{a}}_p = \left(i\Delta_p - \frac{\kappa_p}{2}\right)\bar{a}_p + \sqrt{\eta_p \kappa_p} \bar{a}_{p,\text{in}}, \quad (S2)$$

where the pump tone is detuned from the pump mode by  $\Delta_p = \omega_p - \omega_{o,p}$ , with  $\kappa_p$  and  $\eta_p$  as the pump mode loss rate and external coupling efficiency. *In our experiments, we actively lock the laser frequency to the pump mode resonance, with  $\Delta_p = 0$ .*

The presence of the strong pump field results in an effective interaction Hamiltonian,

$$\hat{H}_{I,\text{eff}}/\hbar = g(\hat{a}_e \hat{a}_o + \hat{a}_e \hat{a}_t^\dagger) + J\hat{a}_t \hat{a}_{tm}^\dagger + h.c., \quad (S3)$$

with multiphoton coupling rate  $g = \bar{a}_p g_0$ . This includes the two-mode-squeezing (TMS) interaction between the Stokes and microwave mode, and beam-splitter (BS) interaction between the anti-Stokes mode and microwave mode, resulting in scattered Stokes and anti-Stokes sidebands that are located on the lower and upper side of the pump tone by  $\Omega_e$  away. Microwave-optics entanglement between the microwave and optical Stokes output field can be achieved via spontaneous parametric down-conversion (SPDC) process due to TMS interaction (28), which is further facilitated by the suppressed anti-Stokes scattering due to the strong coupling between anti-Stokes and TM modes. We can obtain the full dynamics of the intracavity fluctuation field *in the rotating frame of the scattered sidebands and microwave resonance*, which can be described by the quantum Langevin equations (QLE),

$$\dot{\hat{a}}_e = -\frac{\kappa_e}{2}\hat{a}_e - ig\hat{a}_o^\dagger - ig^*\hat{a}_t + \sqrt{\eta_e \kappa_e} \delta \hat{a}_{e,\text{in}} + \sqrt{(1-\eta_e) \kappa_e} \delta \hat{a}_{e,0}, \quad (S4)$$

$$\dot{\hat{a}}_o = \left(i\delta_o - \frac{\kappa_o}{2}\right)\hat{a}_o - ig\hat{a}_e^\dagger + \sqrt{\eta_o \kappa_o} \delta \hat{a}_{o,\text{in}} + \sqrt{(1-\eta_o) \kappa_o} \delta \hat{a}_{o,0}, \quad (S5)$$

$$\dot{\hat{a}}_t = \left(i\delta_t - \frac{\kappa_t}{2}\right)\hat{a}_t - ig^*\hat{a}_e - iJ\hat{a}_{tm} + \sqrt{\kappa_t} \delta \hat{a}_{t,\text{vac}}, \quad (S6)$$

$$\dot{\hat{a}}_{tm} = \left(i\delta_{tm} - \frac{\kappa_{tm}}{2}\right)\hat{a}_{tm} - iJ\hat{a}_t + \sqrt{\kappa_{tm}} \delta \hat{a}_{tm,\text{vac}}, \quad (S7)$$

with  $\kappa_j$  the total loss rate of the individual mode where  $j \in (e, o, t, tm)$ , and  $\eta_k$  the external coupling efficiency of the input field where  $k \in (e, o)$ . We note that, the optical light is only coupled to the TE modes via efficient prism coupling, with effective mode overlap  $\Lambda$  factor included in  $\eta_o$  for simplicity (24).  $\delta_j$  corresponds to the frequency difference between mode  $j$  and scattered sidebands, with  $\delta_o = \omega_{o,p} - \omega_e - \omega_o$  and  $\delta_{t/tm} = \omega_{o,p} + \omega_e - \omega_{t/tm}$ , which are mostly given by FSR and  $\omega_e$  mismatch, with additional contributions from optical mode dispersion and residual optical mode coupling. We note that, for resonant pumping, we have  $\delta_o = -\delta_t$  in the case of absent optical mode dispersion and residual mode coupling. In our experiments, we tune the microwave frequency to match the optical FSR, i.e.  $\omega_e = \omega_{o,p} - \omega_o$ .

The equation of motion of all relevant modes may be represented more economically in the form

$$\dot{\mathbf{v}}(t) = M(t)\mathbf{v}(t) + K\mathbf{f}_{\text{in}}(t), \quad (\text{S8})$$

where we define the vectors of mode and noise operators

$$\begin{aligned} \mathbf{v} &= (\hat{a}_e, \hat{a}_e^\dagger, \hat{a}_o, \hat{a}_o^\dagger, \hat{a}_t, \hat{a}_t^\dagger, \hat{a}_{\text{tm}}, \hat{a}_{\text{tm}}^\dagger)^\top, \\ \mathbf{f}_{\text{in}} &= (\delta\hat{a}_{e,0}, \delta\hat{a}_{e,0}^\dagger, \delta\hat{a}_{e,\text{in}}, \delta\hat{a}_{e,\text{in}}^\dagger, \delta\hat{a}_{o,0}, \delta\hat{a}_{o,0}^\dagger, \delta\hat{a}_{o,\text{in}}, \delta\hat{a}_{o,\text{in}}^\dagger, \delta\hat{a}_{t,\text{vac}}, \delta\hat{a}_{t,\text{vac}}^\dagger, \delta\hat{a}_{\text{tm},\text{vac}}, \delta\hat{a}_{\text{tm},\text{vac}}^\dagger)^\top, \end{aligned} \quad (\text{S9})$$

as well as the matrices that encode the deterministic part of the QLE,

$$M(t) = \begin{pmatrix} -\frac{\kappa_e}{2} & 0 & 0 & -ig(t) & -ig^*(t) & 0 & 0 & 0 \\ 0 & -\frac{\kappa_e}{2} & +ig^*(t) & 0 & 0 & ig(t) & 0 & 0 \\ 0 & -ig(t) & i\delta_o - \frac{\kappa_o}{2} & 0 & 0 & 0 & 0 & 0 \\ ig^*(t) & 0 & 0 & -i\delta_o - \frac{\kappa_o}{2} & 0 & 0 & 0 & 0 \\ -ig(t) & 0 & 0 & 0 & i\delta_t - \frac{\kappa_t}{2} & 0 & -iJ & 0 \\ 0 & ig^*(t) & 0 & 0 & 0 & -i\delta_t - \frac{\kappa_t}{2} & 0 & iJ \\ 0 & 0 & 0 & 0 & -iJ & 0 & i\delta_{\text{tm}} - \frac{\kappa_{\text{tm}}}{2} & 0 \\ 0 & 0 & 0 & 0 & 0 & iJ & 0 & -i\delta_{\text{tm}} - \frac{\kappa_{\text{tm}}}{2} \end{pmatrix}, \quad (\text{S10})$$

and

$$K = \begin{pmatrix} \sqrt{(1-\eta_e)\kappa_e} & \sqrt{\eta_e\kappa_e} & 0 & 0 & 0 & 0 \\ 0 & 0 & \sqrt{(1-\eta_o)\kappa_o} & \sqrt{\eta_o\kappa_o} & 0 & 0 \\ 0 & 0 & 0 & 0 & \sqrt{\kappa_t} & 0 \\ 0 & 0 & 0 & 0 & 0 & \sqrt{\kappa_{\text{tm}}} \end{pmatrix} \otimes \mathbb{1}_2, \quad (\text{S11})$$

which keeps track on which modes the noise acts.

## 2. Input-Output-Theory

In the experiment the pump field is turned on at  $t = 0$  and kept on until  $\tau_{\text{pulse}}$ . For the optical pump pulse with length  $\tau_{\text{pulse}} = 250$  ns (600 ns, see main text), we reject a certain  $\tau_{\text{delay}} = 50$  ns (100 ns) from the beginning of pulse data. Since  $\kappa_p \tau_{\text{delay}} \gtrsim 1$  we may assume that after  $\tau_{\text{delay}}$  the system has approached its steady state and especially that the pump mode is in its steady state. Consequently we may assume that  $g(t > \tau_{\text{delay}}) \simeq g$  is constant over time. One important figure of merit is the multiphoton cooperativity  $C = 4g^2/\kappa_o\kappa_e$ , a measure for coherent coupling versus the microwave and optical dissipation. Efficient entanglement generation can be achieved with complete anti-Stokes scattering suppression, while below the parametric instability threshold, i.e.  $C < 1$ .

The output fields of the CEO device are

$$\mathbf{f}_{\text{out}}(t) = (\hat{a}_{e,\text{out}}(t), \hat{a}_{e,\text{out}}^\dagger(t), \hat{a}_{o,\text{out}}(t), \hat{a}_{o,\text{out}}^\dagger(t))^\top, \quad (\text{S12})$$

which consist of a contribution which was entangled via the coherent interactions  $\mathbf{v}$  and a contribution which has not interacted with the device  $\mathbf{f}_{\text{in}}$ . The output field  $\mathbf{f}_{\text{out}}$  will then propagate to the measurement device and is most economically represented within the framework of input-output theory (46),

$$\mathbf{f}_{\text{out}}(t) = L\mathbf{f}_{\text{in}}(t) - N\mathbf{v}(t), \quad (\text{S13})$$

where we define the matrices

$$N = (N_J, \mathbb{0}_4), \quad \text{with} \quad N_J = \text{Diag}(\sqrt{\eta_e\kappa_e}, \sqrt{\eta_e\kappa_e}, \sqrt{\eta_o\kappa_o}, \sqrt{\eta_o\kappa_o}), \quad (\text{S14})$$

and

$$L = \begin{pmatrix} 0 & 1 & 0 & 0 & 0 & 0 \\ 0 & 0 & 0 & 1 & 0 & 0 \end{pmatrix} \otimes \mathbb{1}_2. \quad (\text{S15})$$

As all modes have reached steady state, the correlations in the output field may be obtained by going to Fourier

domain. Here we commit to following convention of the Fourier transformation

$$\hat{A}(\omega) = \frac{1}{\sqrt{2\pi}} \int_{-\infty}^{\infty} d\omega e^{i\omega t} \hat{A}(t), \quad (\text{S16})$$

with the hermitian conjugate

$$(\hat{A}(\omega))^{\dagger} = \hat{A}^{\dagger}(-\omega). \quad (\text{S17})$$

Note that in this convention e.g.  $[a_e(\omega), a_e^{\dagger}(\omega')] = \delta(\omega + \omega')$  are canonical pairs.

In our experiments, we focus on the correlations between the output propagating spectral modes of frequencies  $\omega_e + \Delta\omega_e$  and  $\omega_o - \Delta\omega_o$  respectively for microwave and optical fields (35, 47). We note that, due to energy conservation in the SPDC process, we only focus on microwave and optical photon pairs around resonances with anti-correlated frequencies, i.e.  $\Delta\omega_e = \Delta\omega_o = \Delta\omega$ . For this reason, we focus on the following vector of output fields in the rotating frame,

$$\mathbf{f}_{\text{out}}(\omega) = (\hat{a}_{e,\text{out}}(\omega), \hat{a}_{e,\text{out}}^{\dagger}(-\omega), \hat{a}_{o,\text{out}}(-\omega), \hat{a}_{o,\text{out}}^{\dagger}(\omega))^{\top}, \quad (\text{S18})$$

in the Fourier domain. From Eq. (S8) we obtain

$$\mathbf{v}(\omega) = \underbrace{[i\omega O - M]^{-1} \cdot K}_{=\mathcal{S}(\omega)} \cdot \mathbf{f}_{\text{in}}(\omega), \quad (\text{S19})$$

with

$$O = \text{Diag}(1, -1, 1, 1) \otimes \sigma_z. \quad (\text{S20})$$

Here we defined the vector of modes

$$\mathbf{v}(\omega) = (\hat{a}_e(\omega), \hat{a}_e^{\dagger}(-\omega), \hat{a}_o(-\omega), \hat{a}_o^{\dagger}(\omega), \hat{a}_t(\omega), \hat{a}_t^{\dagger}(-\omega), \hat{a}_{\text{tm}}(\omega), \hat{a}_{\text{tm}}^{\dagger}(-\omega))^{\top}, \quad (\text{S21})$$

as well as the vector of input fields

$$\mathbf{f}_{\text{in}}(\omega) = (\delta\hat{a}_{e,0}(\omega), \delta\hat{a}_{e,0}^{\dagger}(-\omega), \delta\hat{a}_{e,\text{in}}(\omega), \delta\hat{a}_{e,\text{in}}^{\dagger}(-\omega), \delta\hat{a}_{o,0}(-\omega), \delta\hat{a}_{o,0}^{\dagger}(\omega), \delta\hat{a}_{o,\text{in}}(-\omega), \delta\hat{a}_{o,\text{in}}^{\dagger}(\omega), \delta\hat{a}_{t,\text{vac}}(\omega), \delta\hat{a}_{t,\text{vac}}^{\dagger}(-\omega), \delta\hat{a}_{\text{tm},\text{vac}}(\omega), \delta\hat{a}_{\text{tm},\text{vac}}^{\dagger}(-\omega))^{\top} \quad (\text{S22})$$

in the Fourier domain.

The output fields (see Eq. (S13)) of the CEO device are straight forwardly obtained since in the Fourier domain Eq. (S13) is algebraic,

$$\mathbf{f}_{\text{out}}(\omega) = L\mathbf{f}_{\text{in}}(\omega) + N\mathbf{v}(\omega) = (L + N \cdot [i\omega O - M]^{-1} \cdot K)\mathbf{f}_{\text{in}}(\omega). \quad (\text{S23})$$

The input noise operator correlations are given by,

$$\langle \mathbf{f}_{\text{in}}(\omega) \mathbf{f}_{\text{in}}^{\dagger}(\omega') \rangle = D\delta(\omega + \omega'), \quad (\text{S24})$$

with

$$D = \text{Diag}(\underbrace{\bar{n}_{e,\text{int}} + 1, \bar{n}_{e,\text{int}}}_{\text{bath:e}}, \underbrace{\bar{n}_{e,\text{wg}} + 1, \bar{n}_{e,\text{wg}}}_{\text{waveguide:e}}, \underbrace{1, 0}_{\text{bath:o}}, \underbrace{1, 0}_{\text{detector:o}}, \underbrace{1, 0}_{\text{bath:t}}, \underbrace{1, 0}_{\text{bath:tm}}). \quad (\text{S25})$$

We note that, in our experiments, the microwave waveguide remains in the ground state, with  $\bar{n}_{e,\text{wg}} = 0$ . The spectral correlations of different output field can be simply obtained analytically from

$$\langle \mathbf{f}_{\text{out}}(\omega) \mathbf{f}_{\text{out}}^{\dagger}(\omega') \rangle = \underbrace{\mathcal{S}(\omega) D \mathcal{S}^{\dagger}(-\omega)}_{\tilde{C}_{\mathbf{f}\mathbf{f}^{\dagger}}(\omega)} \delta(\omega + \omega'). \quad (\text{S26})$$

Here we implicitly define the  $4 \times 4$  matrix of output mode correlations with a single entry reading

$$\langle \hat{a}_{\text{out}}(\omega) \hat{b}_{\text{out}}(\omega') \rangle = \tilde{C}_{ab}(\omega) \delta(\omega + \omega'), \quad (\text{S27})$$

where the operators  $\hat{a}_{\text{out}}(\omega), \hat{b}_{\text{out}}(\omega)$  were chosen from components of  $\mathbf{f}_{\text{out}}(\omega)$  in Eq. (S16).

### 3. Covariance Matrix of Filtered Output Fields

We will now consider a situation where we define output field modes from a windowed Fourier transformation. Below we will then show that these are indeed the experimentally observed signals. We start by defining the (dimensionless) hermitian output field quadrature pair (35),

$$\hat{X}_\alpha(\omega_n) = \frac{1}{\sqrt{2T}} \int_{-T/2}^{T/2} d\tau e^{i\omega_n \tau} \hat{a}_{\alpha, \text{out}}(\tau) + \text{h.c.}, \quad (\text{S28})$$

$$\hat{P}_\alpha(\omega_n) = \frac{1}{\sqrt{2T}i} \int_{-T/2}^{T/2} d\tau e^{i\omega_n \tau} \hat{a}_{\alpha, \text{out}}(\tau) + \text{h.c.}, \quad (\text{S29})$$

which meets the canonical commutation relation  $[\hat{X}_\alpha(\omega_n), \hat{P}_\beta(\omega_m)] = i\delta_{nm}\delta_{\alpha\beta}$  where  $\alpha = e, o$ . Due to the finite window of the Fourier transformation, the frequencies  $\omega_n = \frac{2\pi}{T}n$  becomes discrete. The quadrature modes at discrete frequencies  $\omega_n$  can now be rewritten in terms of the (dimensionful) output fields  $\mathbf{f}_{\text{out}}(\omega)$  from Eq. (S23), which are defined in the continuous Fourier domain. Therefore the quadrature operators may be obtained by convolution with the a filter function  $\mathcal{G}(\omega)$

$$\hat{X}_\alpha(\omega_n) = \frac{1}{\sqrt{2}} \int_{-\infty}^{\infty} d\omega \mathcal{G}(\omega_n - \omega) \hat{a}_{\alpha, \text{out}}(\omega) + \text{h.c.} \quad (\text{S30})$$

$$\hat{P}_\alpha(\omega_n) = \frac{1}{\sqrt{2}i} \int_{-\infty}^{\infty} d\omega \mathcal{G}(\omega_n - \omega) \hat{a}_{\alpha, \text{out}}(\omega) + \text{h.c.} \quad (\text{S31})$$

Here the filter is

$$\mathcal{G}(\omega) = \frac{1}{\sqrt{2\pi}} \int_{-\infty}^{\infty} d\tau e^{i\omega\tau} \frac{\mathbb{1}_{[0,T]}(\tau)}{\sqrt{T}} = \sqrt{\frac{2}{\pi T}} \frac{\sin(\omega T/2)}{\omega}, \quad (\text{S32})$$

which is obtained from a Fourier transformation of the unit function  $\mathbb{1}_{[-T/2, T/2]}(t) = 1(0)$  for  $|t| \leq T/2$  ( $|t| > T/2$ ). A bipartite Gaussian state is characterized by the  $4 \times 4$  *covariance matrix* (CM),

$$V_{AB}(\omega_n) = \frac{1}{2} \langle \{ \delta \hat{A}(\omega_n), \delta \hat{B}(\omega_n) \} \rangle. \quad (\text{S33})$$

Here we defined  $\delta \hat{A} = \hat{A} - \langle \hat{A} \rangle$  an operator with zero mean  $\langle \delta \hat{A} \rangle = 0$  and the quadratures from

$$\hat{A}(\omega_n), \hat{B}(\omega_n) \in \{ \hat{X}_e(\omega_n), \hat{P}_e(\omega_n), \hat{X}_o(-\omega_n), \hat{P}_o(-\omega_n) \} \quad (\text{S34})$$

and we also introduced the anti-commutator  $\{ \hat{A}, \hat{B} \} = \hat{A}\hat{B} + \hat{B}\hat{A}$ . Note that the two-mode squeezing interaction results in correlation between frequency reversed pairs on the microwave  $\omega_n$  and the optical site  $\omega_n$ . Since in our setting all first moments  $\langle \hat{A} \rangle = 0$  the evaluation of the covariance matrix in Eq. (S33) boils down to computing spectral correlations which are rewritten as

$$\begin{aligned} \langle \hat{A}(\omega_n) \hat{B}(\omega_n) \rangle &= \int_{-\infty}^{\infty} d\omega \int_{-\infty}^{\infty} d\omega' \mathcal{G}(\omega_n - \omega) \mathcal{G}(\omega_n - \omega') \langle \hat{A}(\omega) \hat{B}(\omega') \rangle \\ &= \int_{-\infty}^{\infty} d\omega \int_{-\infty}^{\infty} d\omega' \mathcal{G}(\omega_n - \omega) \mathcal{G}(-\omega_n - \omega') C_{AB}(\omega) \delta(\omega + \omega') \\ &= \int_{-\infty}^{\infty} d\omega \mathcal{F}(\omega_n - \omega) C_{AB}(\omega), \end{aligned} \quad (\text{S35})$$

where we used the property  $\mathcal{G}(-\omega) = \mathcal{G}(\omega)$  and defined the effective filter  $\mathcal{F}(\omega) = \mathcal{G}(\omega)^2$ . Similar to Eq. (S26), we defined the quadrature correlations

$$C_{AB}(\omega) = (C(\omega))_{AB} = \frac{1}{2} \left( U \tilde{C}_{\mathbf{f}\mathbf{f}^\dagger}(\omega) U^\dagger + (U \tilde{C}_{\mathbf{f}\mathbf{f}^\dagger}(\omega) U^\dagger)^\top \right)_{AB}. \quad (\text{S36})$$

Here the unitary matrix  $U = u \oplus u$ , with

$$u = \frac{1}{\sqrt{2}} \begin{pmatrix} 1 & 1 \\ -i & i \end{pmatrix}, \quad (\text{S37})$$

corresponds to a rotation of the mode operators into quadrature operators  $(\hat{X}_\alpha, \hat{P}_\alpha)^\top = u \cdot (\hat{a}_{\alpha,\text{out}}, \hat{a}_{\alpha,\text{out}}^\dagger)^\top$ . The covariance matrix of the quadrature modes at the discrete frequencies  $\omega_n$  is then obtained exactly by

$$V_{AB}(\omega_n) = \int_{-\infty}^{\infty} d\omega \mathcal{F}(\omega_n - \omega) C_{AB}(\omega), \quad (\text{S38})$$

where the quadrature correlations are convolved with an appropriate filter.

## B. Heterodyne Detection, Added Noise and Filtering

### 1. Heterodyne Measurement

Here we discuss the quadrature extractions from the equivalent linear measurement, e.g. balanced heterodyne detection, with excess added noise (48). In the heterodyne detection, the output field  $\hat{a}_{\text{out}} e^{-i\omega_j t}$  ( $j \in e, o$ ) is mixed with a strong coherent local oscillator field  $\hat{a}_{\text{LO}}(t) = \alpha_{\text{LO}} e^{-i\omega_{\text{LO}} t}$  at a 50:50 beam-splitter, where the output field from the two ports are sent to a balanced photo-detector, which results in a photon current that is proportional to

$$\hat{I}_{\text{out}}(t) = e^{-i\Delta_{\text{LO}} t} \hat{a}_{\text{out}} + \hat{a}_{\text{out}}^\dagger e^{i\Delta_{\text{LO}} t}, \quad (\text{S39})$$

in the limit of strong LO ( $\alpha_{\text{LO}} \gg 1$ ) with  $\Delta_{\text{LO}} = \omega_{\text{LO}} - \omega_j$ . We consider finite measurement interval of time  $T$ , on which we compute the windowed Fourier transformation of  $\hat{I}_{\text{out}}(t)$ ,

$$\begin{aligned} \hat{I}_{\text{out}}(\omega_n) &= \frac{1}{\sqrt{T}} \int_0^T d\tau e^{i\omega_n \tau} \hat{I}_{\text{out}}(\tau) = \frac{1}{\sqrt{T}} \int_0^T d\tau e^{i\omega_n \tau} (e^{-i\Delta_{\text{LO}} \tau} \hat{a}_{\text{out}}(\tau) + e^{i\Delta_{\text{LO}} \tau} \hat{a}_{\text{out}}^\dagger(\tau)) \\ &= a_{\text{out}}(\omega_n - \Delta_{\text{LO}}) + a_{\text{out}}^\dagger(\omega_n + \Delta_{\text{LO}}), \end{aligned} \quad (\text{S40})$$

where in a slight abuse of notation we define the dimensionless output fields  $a_{\text{out}}(\omega_n)$ . The reason why we are explicitly working the windowed Fourier transformation is, that despite being in a steady state during the measurement (see Sec. IB), the Fourier transformed data has a rather broad bandwidth ( $\delta\omega_n = \frac{2\pi}{T} \sim 5\text{MHz}$  for a 200 ns time window) due to the relatively short time of data collection  $T = \tau_{\text{pulse}} - \tau_{\text{delay}} = 200\text{ ns}$  (especially for 250 ns optical pump pulse). In the limit of long measurement times  $T \rightarrow \infty$ , the bandwidth will tend to zero and the following discussion as well as the results in Eq. (S38) will coincide with standard Input-Output treatment in the continuous Fourier domain. In our experiments, we extract the quadratures of microwave and optical output field, by decomposing the heterodyne current spectra, in their real and imaginary parts which yields

$$\hat{I}_{\text{out}}(\omega_n) = \frac{1}{\sqrt{2}} \underbrace{(\hat{X}(\omega_n - \Delta_{\text{LO}}) + \hat{X}(-\omega_n - \Delta_{\text{LO}}))}_{\hat{I}_{X,\text{out}}(\omega_n)} + i \underbrace{[\hat{P}(\omega_n - \Delta_{\text{LO}}) - \hat{P}(-\omega_n - \Delta_{\text{LO}})]}_{\hat{I}_{P,\text{out}}(\omega_n)}, \quad (\text{S41})$$

where we define the quadrature output fields  $\hat{a}_{\text{out}}(\omega_n) = (\hat{X}(\omega_n) + i\hat{P}(\omega_n))/\sqrt{2}$ , in the same way as in Eq. (S28-S29).

So far we have treated the photon current which result from a heterodyne measurement in terms of a time dependent hermitian operator  $\hat{I}_{\text{out}}(t)$ . In an actual experiment the heterodyne current is a real scalar  $I(t)$  quantity which fluctuates in time and between different experimental runs. Taking taking the (fast) Fourier transform of this current and decomposing it in its real and imaginary parts then yields  $I(\omega_n) = I_X(\omega_n) + iI_P(\omega_n)$ . The theory of continuous measurements and quantum trajectories (49, 50) tells us how to connect the measured scalar currents with the current



operators from input-output theory (46)

$$\overline{I_A(\omega_n)I_B(\omega_m)} = \frac{1}{2}\langle\{\hat{I}_{A,\text{out}}(\omega_n), \hat{I}_{B,\text{out}}(\omega_m)\}\rangle, \quad (\text{S42})$$

where we define the statistical average  $\overline{\cdots}$  over many experimental runs.

## 2. Realistic Measurements: Added Noise and Gain

For the vacuum, the noise spectral density for both quadratures, are obtained by

$$S_{AA}(\omega_n) = \langle\hat{A}(\omega_n)\hat{A}(\omega_n)\rangle_{\text{vac}} = \frac{1}{2}, \quad (\text{S43})$$

for the hermitian operator  $\hat{A} = \hat{X}, \hat{P}$ . Note that due to the discreteness of the Fourier domain we do not have a Dirac delta as opposed to Eq. (S27). The noise spectrum of the heterodyne current is defined by  $S_{II}(\omega) \equiv \overline{I(\omega_n)I(\omega_n)} = \langle\hat{I}_{\text{out}}(\omega_n)\hat{I}_{\text{out}}(\omega_n)\rangle$ , where

$$S_{II}(\omega_n) = \frac{1}{2}(S_{XX}(\omega_n - \Delta_{\text{LO}}) + S_{PP}(\omega_n - \Delta_{\text{LO}}) + S_{XX}(\omega_n + \Delta_{\text{LO}}) + S_{PP}(\omega_n + \Delta_{\text{LO}})). \quad (\text{S44})$$

Focusing on the part of the spectrum located around  $\Delta_{\text{LO}}$ ,

$$S_{II}(\omega_n + \Delta_{\text{LO}}) = \frac{1}{2}(S_{XX}(\omega_n) + S_{PP}(\omega_n) + 1), \quad (\text{S45})$$

assuming  $\Delta_{\text{LO}} \gg \kappa_e, \kappa_o$ . This indicates the simultaneous quadratures measurements and added shot noise in the heterodyne measurements, even without experimental imperfections. So far we have focused on the ideal theory of the measurement and disregarded additional unknown sources of noise as well as the connection to the actually measured quantities. In practice, the *decomposed measured quadratures contain additional uncorrelated excess noise*, e.g. due to the added noise in the amplification or due to propagation losses (51). We model this by phenomenologically adding another uncorrelated noise process from an independent thermal reservoir and then multiplying by a gain factor which converts the number of measured photons to the actually monitored voltage. To illustrate this we focus again on a single output port, and with the added noise current  $\hat{I}_{X/P,\text{add}}(\omega_n)$  and the frequency dependent calibration gain  $G_{\text{det}}(\omega_n)$ , where

$$\hat{I}_{X,\text{det}}(\omega_n) = \sqrt{G_{\text{det}}(\omega_n)}(\hat{I}_{X,\text{add}}(\omega_n) + \hat{I}_{X,\text{out}}(\omega_n)), \quad (\text{S46})$$

$$\hat{I}_{P,\text{det}}(\omega_n) = \sqrt{G_{\text{det}}(\omega_n)}(\hat{I}_{P,\text{add}}(\omega_n) + \hat{I}_{P,\text{out}}(\omega_n)). \quad (\text{S47})$$

We thus obtain the detected heterodyne noise spectral density,

$$S_{II,\text{det}}(\omega_n + \Delta_{\text{LO}}) = G_{\text{det}}(\omega_n + \Delta_{\text{LO}})[S_{XX}(\omega_n) + S_{PP}(\omega_n) + \underbrace{1 + S_{I_X I_X,\text{add}}(\omega_n + \Delta_{\text{LO}}) + S_{I_P I_P,\text{add}}(\omega_n + \Delta_{\text{LO}})}_{=2N_{\text{add}}}], \quad (\text{S48})$$

where we define the spectra of the added noise  $S_{I_O I_O,\text{add}}(\omega_n) = \langle\hat{I}_{O,\text{add}}(\omega_n)\hat{I}_{O,\text{add}}(\omega_n)\rangle$ . The added noise  $N_{\text{add}}$  includes the excess vacuum noise from heterodyne measurement and the additional uncorrelated noise. Note that here the factor  $\frac{1}{2}$  was absorbed in the detections gains. The gain  $G_{\text{det}}(\omega_n)$  can be simply obtained on both microwave and optical side, from the cold measurements (optical pump off) with a known background. We note that, Eq. (S48) lays the foundation of microwave and optical calibrations in our CEO device.

In our experiments, we place the LO on opposite sites around the mode resonances, i.e.,

$$\Delta_{\text{LO},e} = -\Omega_{\text{IF}}, \quad \Delta_{\text{LO},o} = \Omega_{\text{IF}}, \quad (\text{S49})$$

where  $\Omega_{\text{IF}} > 0$  is the intermediate frequency for down-mixing. The heterodyne output field can be obtained similar

to Eq. (S40),

$$\begin{aligned}\hat{I}_{\text{out,e}}(\omega_n + \Omega_{\text{IF}}) &= \frac{1}{\sqrt{2}}[(\hat{X}_e(-\omega_n) + \hat{X}_e(\omega_n + 2\Omega_{\text{IF}}) + i(-\hat{P}_e(-\omega_n) + \hat{P}_e(\omega_n + 2\Omega_{\text{IF}}))], \\ \hat{I}_{\text{out,o}}(\omega_n + \Omega_{\text{IF}}) &= \frac{1}{\sqrt{2}}[\hat{X}_o(-\omega_n - 2\Omega_{\text{IF}}) + \hat{X}_o(\omega_n) + i(-\hat{P}_o(-\omega_n - 2\Omega_{\text{IF}}) + \hat{P}_o(\omega_n))],\end{aligned}\quad (\text{S50})$$

with noise spectrum given by,

$$\begin{aligned}S_{II,e}(\omega_n + \Omega_{\text{IF}}) &= \frac{1}{2}(S_{X_e X_e}(-\omega_n) + S_{P_e P_e}(-\omega_n)) + N_{e,\text{add}}, \\ S_{II,o}(\omega_n + \Omega_{\text{IF}}) &= \frac{1}{2}(S_{X_o X_o}(\omega_n) + S_{P_o P_o}(\omega_n)) + N_{o,\text{add}}.\end{aligned}\quad (\text{S51})$$

We note that, Eq. (S50) is adopted for *field quadrature extraction (including the added noise) from the heterodyne measurement*, which reveals correlations in the quadrature histogram [cf. Fig.4 in the main text]. Despite of the *reversed sign in the expected field quadratures, microwave and optical output photons appear at the same frequency in the noise spectrum, i.e.  $\omega_n + \Omega_{\text{IF}}$*  [cf. Fig.2 d,e in the main text].

### 3. Covariance Matrix from Realistic Heterodyne Measurements

Here we briefly explain the procedure of the covariance matrix reconstruction from the heterodyne measurements. *The cross correlations of the detected heterodyne current spectra* can be obtained via,

$$\mathcal{D}_{AB}(\omega_n) = \overline{\delta I_{A,\text{det}}(\omega_n + \Omega_{\text{IF}}) \delta I_{B,\text{det}}(\omega_n + \Omega_{\text{IF}})}, \quad (\text{S52})$$

where we define the centered current  $\delta I_{O,\text{det}} = I_{O,\text{det}} - \overline{I_{O,\text{det}}}$ , with

$$I_{O,\text{det}}(\omega_n) \in \{I_{X_e,\text{det}}(\omega_n), I_{P_e,\text{det}}(\omega_n), I_{X_o,\text{det}}(\omega_n), I_{P_o,\text{det}}(\omega_n)\}. \quad (\text{S53})$$

Similar to Eq. (S42), we can obtain

$$\begin{aligned}\mathcal{D}_{AB}(\omega_n) &= \frac{1}{2} \langle \{ \delta \hat{I}_{A,\text{det}}(\omega_n + \Omega_{\text{IF}}), \delta \hat{I}_{B,\text{det}}(\omega_n + \Omega_{\text{IF}}) \} \rangle \\ &= \sqrt{G_{A,\text{det}}(\omega_n + \Omega_{\text{IF}}) G_{B,\text{det}}(\omega_n + \Omega_{\text{IF}})} \underbrace{\left[ \frac{1}{2} \langle \{ \delta \hat{A}(\omega_n), \delta \hat{B}(\omega_n) \} \rangle + N_{AB,\text{add}} \right]}_{=V_{AB}(\omega_n)},\end{aligned}\quad (\text{S54})$$

where we define the diagonal added noise matrix  $N_{AB,\text{add}} = (N_{\text{add}})_{AB} = N_{A,\text{add}} \delta_{AB}$  with the calibrated added noise  $N_{\text{add}}$  and detection gain  $G_{A,\text{det}}$ . *This equation establishes how the covariance matrix of the quadrature operators [cf. Eq. (S38)] is reconstructed from heterodyne measurements, and how they can be compared with the results from idealized standard input-output theory Eq. (S33).* For simplicity, in the main text we define the *total measured covariance matrix including the added noise* as,

$$V_{AB,\text{meas}}(\omega_n) = \mathcal{D}_{AB}(\omega_n) / \sqrt{G_{A,\text{det}}(\omega_n + \Omega_{\text{IF}}) G_{B,\text{det}}(\omega_n + \Omega_{\text{IF}})}, \quad (\text{S55})$$

with  $V_{AB,\text{meas}}(\omega_n) = V_{AB}(\omega_n) + N_{AB,\text{add}}$ .

We note that, in principle the location of both LOs can be arbitrary. As evident in Eq. S54, our choice of the LO configuration, i.e.  $\Delta_{\text{LO,e}} = -\Delta_{\text{LO,o}} = -\Omega_{\text{IF}}$ , offers a simple solution to the quantification of the broadband quantum correlations, considering the limited detection bandwidth, frequency dependent gain, or microwave cavity frequency shift, which may result in the loss of quantum correlations during quadrature extractions in heterodyne measurements due to imperfect frequency matching.

### C. Entanglement Detection

#### 1. Duan Criterion

We will now discuss how to show that the photons outgoing microwave and optical photons are indeed inseparable or entangled. Our starting point is the covariance matrix which we defined in Eq. (S33) and measured as outlined in Eq. (S54). The experimentally measured covariance matrix is of the form

$$V = \begin{pmatrix} V_e & V_{eo} \\ V_{eo} & V_o \end{pmatrix} = \begin{pmatrix} V_{11} & 0 & \tilde{V}_{13} & \tilde{V}_{14} \\ 0 & V_{11} & \tilde{V}_{14} & -\tilde{V}_{13} \\ \tilde{V}_{13} & \tilde{V}_{14} & V_{33} & 0 \\ \tilde{V}_{14} & -\tilde{V}_{13} & 0 & V_{33} \end{pmatrix}. \quad (\text{S56})$$

Since there is no single mode squeezing we have  $V_{22} = V_{11}$  and  $V_{44} = V_{33}$ . For simplicity we have omitted the frequency argument  $\omega_n$  of component. What we describe in the following will have to be repeated for every frequency component. The off-diagonal part in the covariance matrix which encodes the two-mode squeezing can be written as

$$V_{eo} \simeq V_{13}(\sin(\theta)\sigma_x + \cos(\theta)\sigma_z), \quad (\text{S57})$$

where we define  $V_{13} = (\tilde{V}_{14}^2 + \tilde{V}_{13}^2)^{1/2}$  and the mixing angle  $\tan(\theta) = \tilde{V}_{14}/\tilde{V}_{13}$ . In our experimental setting  $\tilde{V}_{14}$  maybe non zero e.g. due to small finite detunings  $\delta_o$ . For the detection of inseparability, we employ the criterion introduced by Duan, Gidke, Cirac and Zoller (31). This criterion states that if one can find local operations  $U_{\text{loc}} = U_e \otimes U_o$  such that the joint amplitude variance of  $\hat{X}_+ = (\hat{X}_e + \hat{X}_o)/\sqrt{2}$  break the inequality,

$$\Delta X_+^2 = \langle U_{\text{loc}}^\dagger \hat{X}_+^2 U_{\text{loc}} \rangle < 1/2, \quad (\text{S58})$$

then the state is inseparable and, thus it must be concluded that it is entangled.

In this setting, it is enough to choose the local operations  $U_{\text{loc}} = U_e U_o$  to be a passive phase rotation on the optical mode only, with  $U_e = \mathbb{1}$  and  $U_o = e^{-i\varphi \hat{a}_o^\dagger \hat{a}_o}$ , and phase rotation angle  $\varphi$ . In the space of covariance matrices, this corresponds to the (symplectic) transformation  $S_\varphi = \mathbb{1}_2 \oplus R_\varphi$ , where we define the rotation matrix,

$$R_\varphi = \begin{pmatrix} \cos(\varphi) & \sin(\varphi) \\ -\sin(\varphi) & \cos(\varphi) \end{pmatrix}. \quad (\text{S59})$$

The local rotation of the phase  $V(\varphi) = S_\varphi V S_\varphi^\top$  will act on the off diagonal part of the covariance matrix as,

$$V_{ea}(\varphi) = V_{13}(\cos(\theta - \varphi)\sigma_z + \sin(\theta - \varphi)\sigma_x). \quad (\text{S60})$$

With these local rotations the joint amplitude variance becomes

$$\Delta X_+^2(\varphi) = \langle (\hat{X}_e + \hat{X}_o \cos(\varphi) + \hat{P}_o \sin(\varphi))^2 \rangle / 2 = V_{11} + V_{33} + 2V_{13} \cos(\theta - \varphi). \quad (\text{S61})$$

We can similarly define the joint quadrature  $\hat{P}_- = (\hat{P}_e - \hat{P}_o)/\sqrt{2}$ , where  $\Delta P_-^2(\varphi) = \Delta X_+^2(\varphi)$ . The variance of the joint quadratures  $\Delta X_+^2(\varphi)$  and  $\Delta P_-^2(\varphi)$  is minimized at the angle  $\varphi_- = \theta - \pi$

$$\Delta_{\text{EPR}}^- = \Delta X_+^2(\varphi_-) + \Delta P_-^2(\varphi_-) = 2(V_{11} + V_{33} - 2V_{13}), \quad (\text{S62})$$

which corresponds to the two-mode squeezing of microwave and optical output field, and the microwave-optics entanglement. In addition, the joint quadrature variance is maximized at the angle  $\varphi_+ = \theta$  and we obtain

$$\Delta_{\text{EPR}}^+ = \Delta X_+^2(\varphi_+) + \Delta P_-^2(\varphi_+) = 2(V_{11} + V_{33} + 2V_{13}), \quad (\text{S63})$$

which corresponds to the anti-squeezing.

## 2. Logarithmic Negativity, Purity and Effective Squeezing

A mixed entangled state can be quantified by the logarithmic negativity,

$$E_N = \max[0, -\log(2\zeta_-)], \quad (\text{S64})$$

where  $\zeta_-$  is the smaller symplectic eigenvalue of the partially transposed covariance matrix and can be obtained analytically

$$\zeta_-^2 = \frac{S - \sqrt{S^2 - 4\det(V)}}{2}, \quad (\text{S65})$$

where we defined the Seralian invariant  $S = \det(V_e) + \det V_o + 2\det(V_{eo})$ . Furthermore the purity of a bipartite Gaussian state is given by

$$\rho = \frac{1}{4\sqrt{\det(V)}}, \quad (\text{S66})$$

with  $\rho = 1$  for a pure state i.e. the vacuum state.

The CM in normal form:

$$V = \begin{pmatrix} V_{11} & 0 & \tilde{V}_{13} & 0 \\ 0 & V_{11} & 0 & -\tilde{V}_{13} \\ \tilde{V}_{13} & 0 & V_{33} & 0 \\ 0 & -\tilde{V}_{13} & 0 & V_{33} \end{pmatrix}, \quad (\text{S67})$$

can be expressed as a two-mode squeezed thermal state with effective thermal noise photon number in two modes  $n_i$  and effective squeezing parameter  $r$ . As a function of CM elements, these numbers are calculated as (53)

$$\begin{aligned} V_{11} &= \frac{(1 + n_1 + n_2) \cosh(2r) + (n_1 - n_2)}{2} \\ V_{33} &= \frac{(1 + n_1 + n_2) \cosh(2r) - (n_1 - n_2)}{2} \\ V_{13} &= \frac{(1 + n_1 + n_2) \sinh(2r) \cos \phi}{2}. \end{aligned} \quad (\text{S68})$$

## II. EXPERIMENTAL SETUP

The experimental setup is shown and described in SI Fig. S1. The laser is split into three parts, including an optical pulsed pump at frequency  $\omega_p$ , a continuous signal at  $\omega_p - \text{FSR}$  for the 4-port calibration (cf. SI III), and a continuous local oscillator (LO) at  $\omega_p - \text{FSR} + \Omega_{\text{IF}}$  for the optical heterodyne detection. The optical signal and pump pulse are sent to the optical resonator of the electro-optical device (DUT) and the reflected light (with pump pulse rejected by a filter cavity) is combined on a 50:50 beam splitter with the optical local oscillator with subsequent balanced photodetection.

Microwave input signals are attenuated at different temperature stages of the dilution refrigerator (4 K: 20 dB, 800 mK: 10 dB, 10 mK: 20 dB), and sent to the coupling port of the microwave cavity of the DUT. The reflected microwave signal is amplified and can then either be mixed with a microwave local oscillator of frequency  $\text{FSR} - \Omega_{\text{IF}}$  and subsequently digitized, or directly measured by a vector network analyzer or a spectrum analyzer.

We note that, *the optical LO is on the right side of optical mode, while the microwave LO is on the left side of the microwave mode, with  $\Omega_{\text{IF}}/2\pi = 40$  MHz*. More details are in the caption of Fig. S1.

## III. SETUP CHARACTERIZATION AND CALIBRATION

In the main manuscript, we show results from two different sets of optical modes shown in Fig. S2. The main difference between these mode sets is the amount of suppression of the anti-Stokes scattering rate compared to Stokes scattering rate given by scattering ratio  $\mathcal{S}$ , which depends on the mode hybridization of the anti-Stokes mode (14,

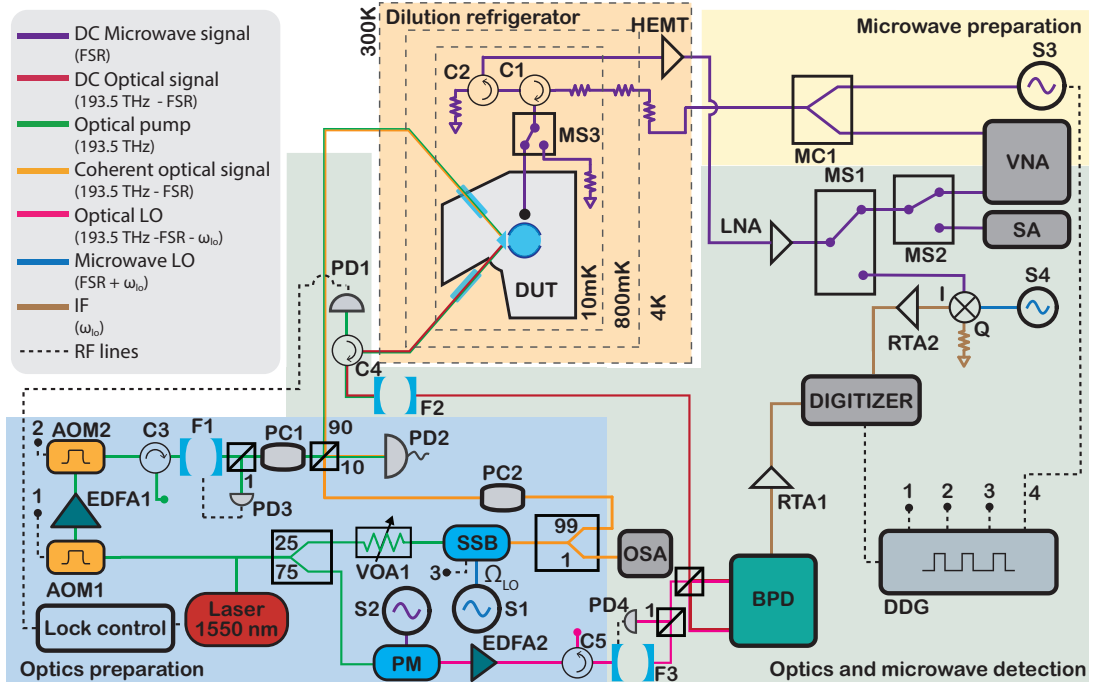


Figure S1. **Experimental setup for two-mode squeezing measurements.** A tunable laser at frequency  $\omega_p$  is initially divided equally in two parts - the optical pump and the optical signal together with the optical local oscillator (LO). Light from the optical pump path is pulsed via an acousto-optic modulator (AOM1) which produces and shapes ns-pulses for amplification via an Erbium-doped fiber amplifier (EDFA). The output from the EDFA is filtered in time (via AOM2) to remove the amplified spontaneous emission (ASE) noise and in frequency via filter F1 ( $\sim 50$  MHz linewidth with 15 GHz FSR) to remove any noise at the optical signal frequency. The filter F1 is locked to the transmitted power by taking 1% of the filter transmission measured via photodiode PD3. The polarization of the final output is controlled via polarization controller PC1 before being mixed with the optical signal via a 90-10 beam splitter and sent to the dilution refrigerator (DR). The 10% output from the beam splitter is monitored on a fast detector PD2 to measure the optical pump pulse power. The other half of the laser is divided into two parts - 25% for the optical signal and 75% for the optical LO. The signal part is sent first to a variable optical attenuator VOA1 to control the power and then to a single sideband modulator SSB which produces the optical signal frequency at  $\omega_p - \text{FSR}$  and suppresses the tones at  $\omega_p$  and  $\omega_p + \text{FSR}$ . 1% of the optical signal is used to monitor the SSB suppression ratio via an optical spectrum analyzer OSA and 99% is sent to the DR with polarization control via PC2. The optical LO is produced via a phase modulator PM and detuned by  $\omega_{\text{IF}}/2\pi = 40$  MHz. As the PM produces many sidebands, the undesired sidebands are suppressed via filter F3 ( $\sim 50$  MHz linewidth with 15 GHz FSR), reflection is rejected by circulator C5. F3 is temperature-stabilized and locked to the transmitted power similar to F1. The optical LO is also amplified via EDFA2 before the optical balanced heterodyne. In the DR, the light is focused via a gradient-index (GRIN) lens on the surface of the prism and coupled to the optical whispering gallery mode resonator (WGMR) via evanescent coupling. Polarization controllers PC1 and PC2 are adjusted to efficiently couple to the TE modes of the optical WGMR. The output light is sent in a similar fashion to the collection GRIN lens. Outside the DR, the optical pump is filtered via filter F2 (similar to F3). The reflected light from F2 is redirected via C4 to be measured with photodiode PD1 which produces the lock signal for the laser to be locked to optical WGMR. The filtered signal is finally mixed with the optical LO and measured with a high speed balanced photo-diode BPD (400 MHz). The electrical signal from the BPD is amplified via room temperature amplifier RTA1 before getting digitized. On the microwave side, the signal is sent from the microwave source S3 which is connected to the digital delay generator (DDG) for accurately timed pulse generation (or from the vector network analyzer VNA for microwave mode spectroscopy) to the fridge input line via the microwave combiner (MC1). The input line is attenuated with attenuators distributed between 4 K and 10 mK accumulating to 50 dB in order to suppress room temperature microwave noise. Circulator C1 and C2 shield the reflected tone from the input signal and lead it to the amplified output line. The output line is amplified at 4 K by a HEMT-amplifier and then at room temperature again with a low noise amplifier (LNA). The output line is connected to microwave switch MS1 and MS2, to select between an ESA, a VNA or a digitizer measurement via manual downconversion using MW LO S4 (40 MHz detuned). Lastly, switch MS3 allows to swap the device under test (DUT) for a temperature  $T_{50\Omega}$  controllable load, which serves as a broad band noise source in order to calibrate the microwave output line's total gain and added noise.

28). The first set of optical mode (Fig. S2A) from which we show most of our main results (main text Fig. 2, 3 and supplement Fig. S13A) has  $\mathcal{S} = -10.3$  dB on-resonance with an effective FSR = 8.799 GHz. The last power sweep shown in Fig. S13B is measured with a second set of optical modes with a lower  $\mathcal{S} = -3.1$  dB and a different effective FSR = 8.791 GHz (Fig. S2B). Despite it being the same optical resonator, the FSR for the second set of optical modes

is slightly different, because of partial hybridisation of the optical pump mode which alters the working FSR between the optical pump and signal mode, see Fig. S2.

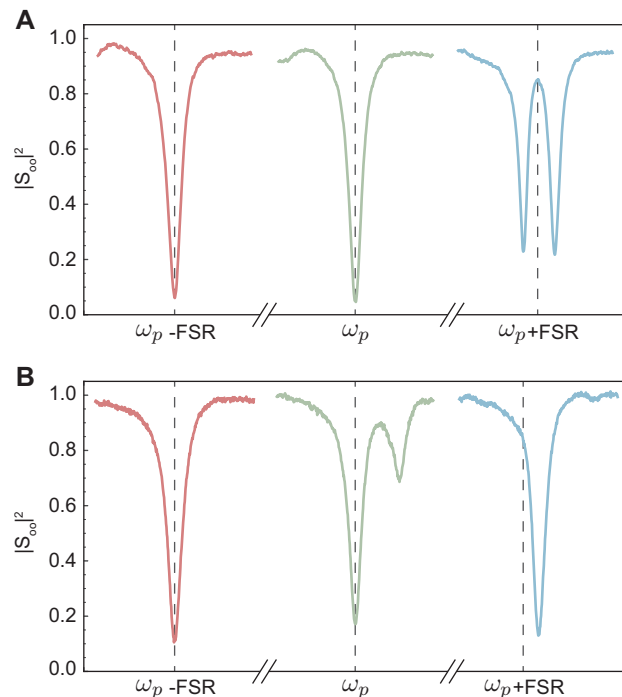


Figure S2. **Optical mode spectra in reflection.** Normalized reflection intensity  $|S_{oo}|^2$  spectra of optical modes  $\hat{a}_o$ ,  $\hat{a}_p$  and  $\hat{a}_t$  in red, green and blue respectively. (A and B) shows the optical mode spectra of the first and second set of modes with the anti-Stokes and Stokes scattering ratio  $\mathcal{S} = -10.3$  dB and  $-3.1$  dB respectively. The dashed line marks the effective FSR between the pump mode  $\hat{a}_p$  and the optical mode  $\hat{a}_o$ . The participation anti-Stokes optical mode  $\hat{a}_t$  is suppressed for this effective FSR as marked by the dashed line over the blue mode.

In the following, we carefully calibrate the added noise due to the microwave detection chain at both these working FSRs (since microwave mode is parked at the working FSR). The added noise can be slightly different depending on frequency of measurement due to impedance mismatch and reflections between components in the microwave detection.

### A. Microwave Added Noise Calibration

In the following, we carefully calibrate the microwave detection chain at both frequencies. We use a combination of a  $50\ \Omega$  load, a thermometer and a resistive heater that are all thermally well connected in one packaged unit. We attach this calibration unit to the microwave output line in place of the microwave cavity via a latching switch at the millikelvin temperature stage. We heat the  $50\ \Omega$  load with the resistive heater and record the amplified noise spectrum  $P_{50\Omega}(\omega)$  as a function of temperature of the load  $T_{50\Omega}$ . The output noise detected over a bandwidth  $B$ ,  $P_{50\Omega}$ , as a function of  $T_{50\Omega}$  is given as,

$$P_{50\Omega} = \hbar\omega_e GB \left[ \frac{1}{2} \coth \left( \frac{\hbar\omega_e}{2k_B T_{50\Omega}} \right) + N_{e,\text{add}} \right], \quad (\text{S69})$$

with  $\omega_e$  the center microwave frequency,  $N_{e,\text{add}}$  ( $G$ ) the input referred added noise (total gain) of the effective microwave detection chain, and  $k_B$  the Boltzmann constant.

A bandwidth of 11 MHz is selected to calculate  $N_{e,\text{add}}$  and  $G$  at the relevant frequency. For  $\omega_e/(2\pi) = 8.799$  GHz, we show the detected noise  $N_{e,\text{det}}$  as a function of  $T_{50\Omega}$  in Fig. S3 along with a fit using Eq. S69, with two fitting parameters  $G$  and  $N_{e,\text{add}}$ . We note that, at  $T_{50\Omega} = 0$  K,  $N_{e,\text{det}} = N_{e,\text{add}} + 0.5$ . Table S1 (third row) shows the obtained added noise and gain for both frequencies of interest, i.e.  $\omega_e/(2\pi) = 8.799$  GHz and  $\omega_e/(2\pi) = 8.791$  GHz.

Figure S4 shows similarly obtained  $N_{e,\text{det}}$  and  $G$  over a larger range of microwave detection frequencies using a smaller resolution bandwidth. We assign the observed variation to expected small impedance mismatches in the

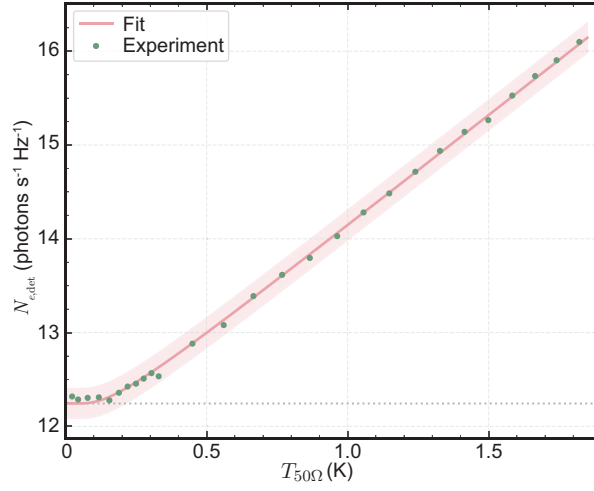


Figure S3. **Characterization of the added noise in the microwave detection chain.** Measured output noise from a  $50\,\Omega$  calibration load as a function of its temperature  $T_{50\Omega}$ . The measured noise is plotted in units of photons as  $N_{det}^{50\Omega} = P_{50\Omega}/(\hbar\omega_e GB)$ . The dashed line at the bottom represents the fitted vacuum noise level in addition to the added noise. The red line and shaded region represents the fit and the 95% confidence interval around it.

microwave detection chain. Importantly, over the comparably small emission bandwidth  $\sim 10$  MHz of the device and bandwidth of the pulses used, the parameters vary by only  $<1\%$ . The uncertainty due to this small variance in the added noise calibration is taken into account and propagated to calculate the systematic error bars shown in the main text.

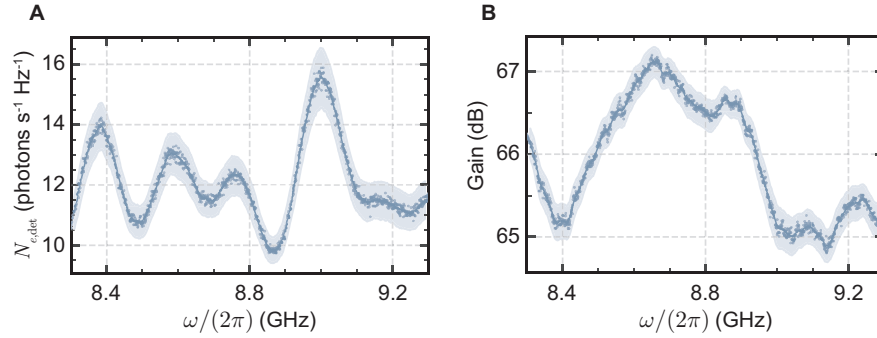


Figure S4. **Microwave added noise and gain spectra.** Measured detection noise  $N_{e,det} = N_{e,add} + 0.5$  (A) and gain  $G$  (B) as a function of detection frequency obtained from fits similar to Fig. S3 but with a 1 MHz resolution bandwidth. The shaded area represents the  $2\sigma$  error in the two fit parameters.

The microwave detection chain is identical for the signals from the  $50\,\Omega$  load and the microwave cavity reflection, except for a small difference in cable length to the switch. We independently determine a difference of  $\sim 0.5$  dB in cable loss by measuring the microwave reflection from the microwave cavity and from the microwave switch directly before it. Including this additional cable losses, the gain decreases accordingly for the reflected microwave detection, shown in Table S1 (fourth row). Since this is a loss before the first amplifier it directly affects the added noise as well, as shown in Table S1 and in agreement with Frii's law.

Finally, we consider an additional uncertainty due to the expected temperature sensor inaccuracy of 2.5%. Although this does not change the final  $N_{e,add}$  and  $G$ , it increases the error bars as shown in Table S1 (fifth row). The error calculated in this section contributes to the *systematic error* reported in the main text.

## B. Optical Added Noise

Optical added noise is calculated via 4-port calibration of our device (14). In this calibration, we measure the coherent response of our device through its 4 ports - optical input/output and microwave input/output. Sending



Table S1. The added noise and gain in microwave detection chain ( $1\sigma$  errors shown)

Detection Chain	8.799 GHz		8.791 GHz	
	$N_{e,\text{add}}$	G (dB)	$N_{e,\text{add}}$	G (dB)
50Ω load (with fitting error)	$11.74 \pm 0.08$	$66.67 \pm 0.02$	$11.76 \pm 0.09$	$66.72 \pm 0.03$
MW cavity (including cable loss)	$13.09 \pm 0.09$	$66.20 \pm 0.02$	$13.16 \pm 0.10$	$66.23 \pm 0.03$
MW cavity (including temperature sensor uncertainty)	$13.09 \pm 0.33$	$66.20 \pm 0.12$	$13.16 \pm 0.34$	$66.23 \pm 0.12$

an optical (or microwave) signal to the DUT in combination with a strong pump leads to stimulated parametric down-conversion (StPDC) process, which generates an amplified microwave (optical) coherent signal. We measure the 4  $S$ -parameters of our device - microwave reflection ( $S_{11}$ ), optics reflection ( $S_{22}$ ), microwave to optics transmission ( $S_{21}$ ) and optics to microwave transmission ( $S_{12}$ ). The mean transduction efficiency between microwave and optics of the DUT is then calculated as,

$$\eta = \sqrt{\frac{S_{12}S_{21}}{S_{11}S_{22}}}. \quad (\text{S70})$$

We use the transduction efficiency and  $N_{e,\text{add}}$  in the microwave detection chain from Sec. III A to calculate the optical added noise.  $N_{e,\text{add}}$  is firstly used to calculate the effective microwave detection gain (different from the one in Sec. III A, because the microwave detection line used for the 4-port calibration uses analog downconversion and digitization, while the thermal calibration uses an SA, see Fig. S1). The microwave gain, along with the (off-resonant) microwave reflection measurement, is used to calculate the microwave input loss. We can obtain the microwave signal power at the DUT, which allows us to calculate the output optical power of the DUT using the transduction efficiency. In conjunction with the measured output power at the end of the detection chain, the losses in the optical detection path and hence, the effective added noise with respect to the optical port of the DUT can be calculated. The calculated optical added noise is  $N_{o,\text{add}} = 5.54 \pm 0.21 (7.42 \pm 0.22)$  for  $\omega_e = 8.799$  GHz (8.791 GHz), corresponding to a net detection efficiency of  $1/(N_{o,\text{add}} + 1) \approx 15\%$ .

Although, in this experiment, we did not separately calibrate the optical losses and the optical heterodyne efficiency, we can use the optical losses from Ref. (14), where the same setup was used. The losses from the optical filter cavity (about 4 dB) and other losses due to out-coupling of light from the device back into the optical fiber, as well as various fiber connections (about 3 dB) amount to about 7 dB. The net detection efficiency was improved from Ref. (14) mostly by optimizing the optical LO power bringing the heterodyne efficiency to 75%.

#### IV. DATA TREATMENT

In this section, we describe all the steps for the data treatment in detail, which includes the time domain analysis (Sec. IV A), the pulse post-selection due to setup drift (Sec. IV B), the frequency domain analysis (Sec. IV C), and the quadrature correlations (Sec. IV D).

##### A. Time-domain Analysis

Both microwave and optical signals are detected via heterodyne detection by mixing with a strong local oscillator that is  $\sim 40$  MHz detuned from respective mode resonance. The output heterodyne signals are digitized using a digitizer at 1 gigasamples/second. First, we digitally downconvert the digitized data at  $\omega_{\text{IF}} = 40$  MHz. This yields the two quadratures  $I_{X_{e/o},\text{det}}(t)$  and  $I_{P_{e/o},\text{det}}(t)$  of the microwave or optical output signal record with 40 MHz resolution bandwidth (using 25 ns time resolution). Fig. S5 shows the calibrated output power ( $I_{X_{e/o},\text{out}}^2 + I_{P_{e/o},\text{out}}^2$ ) [cf. Eq. S50] and the phase ( $\arctan(I_{X_{e/o},\text{out}}/I_{P_{e/o},\text{out}})$ ) from a single pulse sequence. This includes the stochastic SPDC signals from a strong pump pulse, and the coherent StPDC signal from a weaker pump pulse together with a coherent microwave signal for calibration purposes. The SPDC signal produced by the first strong pulse is labeled by the shaded region for one single pulse, and the averaged output power over many pulses is shown in main text Fig. 2. The coherent microwave reflection and stimulated parametric downconverted optical signal are adopted to obtain the



phases during the pulse. We record this measured phase in both signal outputs during the second optical pump pulse for phase-drift correction in later post processing.

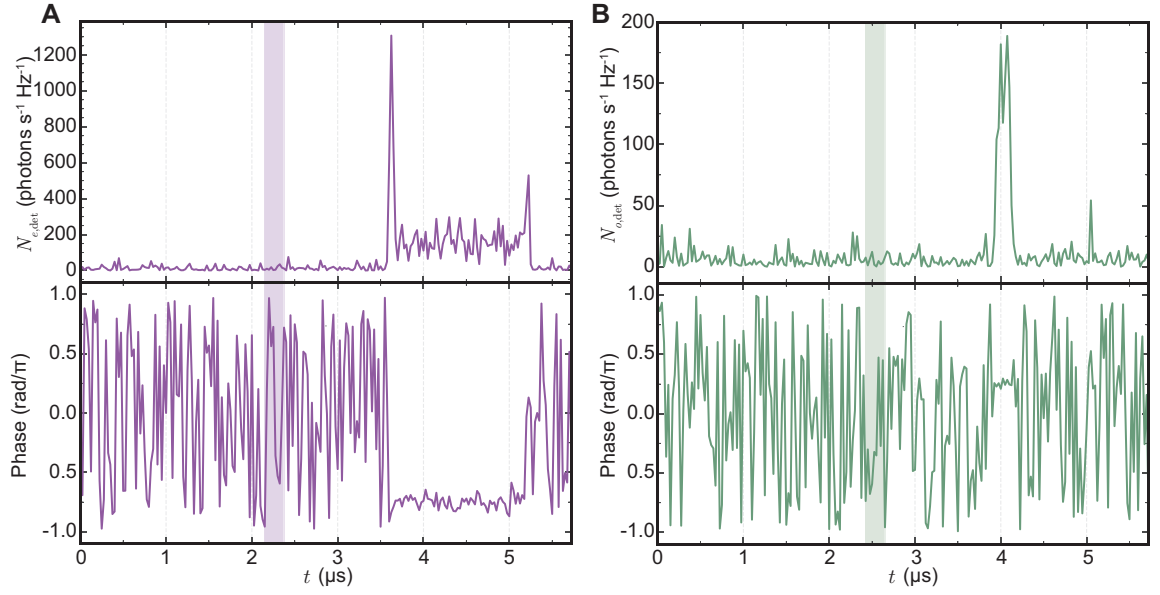


Figure S5. **Downconverted output signal for a single measured pulse sequence.** (A and B) show the measured microwave and optical output signal downconverted at 40 MHz. The shaded part in each case shows the region of the SPDC signal (the first optical pump pulse). For a single pulse, the SNR of a SPDC signal is too small to be seen. However, during the second optical pump pulse, a coherent response is seen in both signal outputs where the phase can be measured with high SNR for each single shot.

In order to determine the accuracy of a phase correction for the first pump pulse based on the phase measurement during the second pump pulse, we send a continuous microwave signal during both pump pulses and recorded the phase of the converted optical pulse during the first and the second optical pump pulse. Fig. S6 shows the phase difference between the first and second optical pump pulse for 2500 trials along with a normal distribution fit. The fit variance for the distribution is 0.17 rad. On a similar set of model data, applying a random phase variation of 0.17 rad results in about 1.5-2.0% loss of correlations [cf. Sec. IV D], whereas, we observe about 6-8% loss of correlations in the experiments. The imperfection in phase correction does not completely explain the decreased quantum correlations, which might be due to other experimental instabilities, especially the optical pump laser lock.

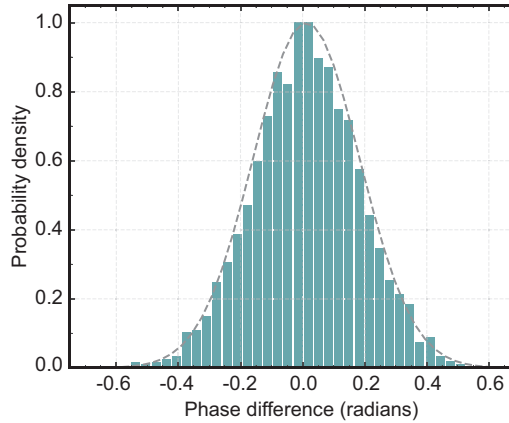


Figure S6. **Accuracy of phase correction scheme.** The histogram shows the difference in the measured phase between the first and second optical pump pulse. Since we correct the phase in the first pump pulse based on the measured optical phase of the second optical pump pulse, the difference shows the limitations of this method. The grey dashed line is a normal distribution fit with variance 0.17 rad.

## B. Pulse Post-selection

In our experiments, we use three temperature-stabilized optical filters, which may drift slowly in time. Two of them are used in the optical heterodyne detection. In the signal path, one filter (F2 in Fig.S1) is used to filter the optical signal while reject the strong optical pump. In the LO path, one filter (F3 in Fig.S1) is used to obtain a clean optical LO tone, which is generated by an electro-optic phase modulator (which produces multiple sidebands) and then amplified using an EDFA (which produces excess amplified spontaneous emissions).

The slow filter drifts can be identified from the amplitude of the coherent optical signal produced via stimulated parametric downconversion during the second optical pump pulse, which drops due to either the decreased transmission after F2 or the reduced LO power after the F3. This is evident in the histogram of the converted optical power during the second optical pump pulse as shown in Fig. S7A. The histogram is not symmetric and has a tail at the lower end. To filter out the instances of drifted heterodyne detection, we select a threshold (in this case marked by a dashed line in Fig S7) and remove all pulses below the selected threshold along with 20 neighboring pulses (10s in total time) before and after such instance. These numbers are chosen according to the filter drift and the filter temperature lock time-scales. After such filtering, usually about 10% of the data is removed and the histogram of the converted optical power during the second optical pump pulse becomes symmetric as shown in Fig. S7B.

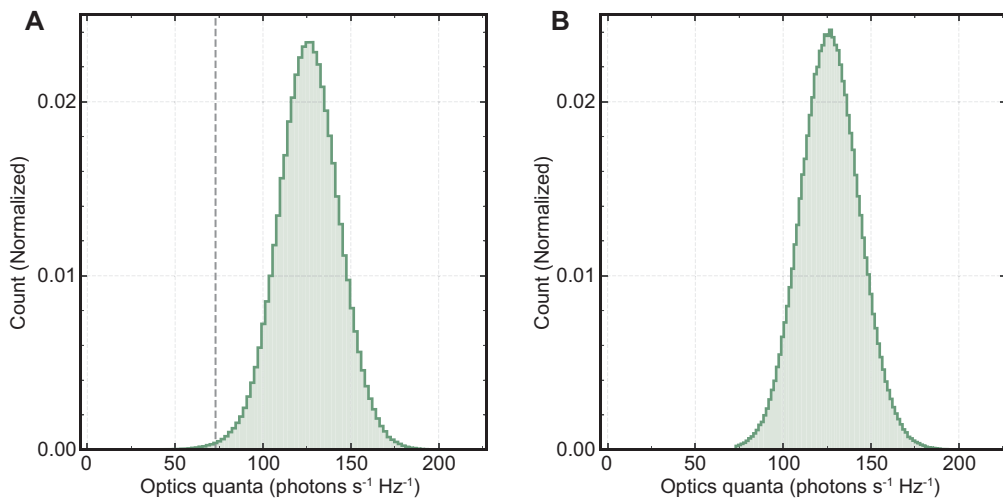


Figure S7. **Histogram of the converted optical power.** The measured coherent optical power during the second optical pump pulse depends on the optical heterodyne gain and the received optical signal power. Both of these values can drift depending on the experimental setup's stability. (A) shows the normalized histogram of this measured optical power over all the collected pulses. The histogram has a tail on the lower end owing to the times when the heterodyne setup drifted. Filtering the points which do not meet a selected threshold (shown by the grey dashed line in panel A), we remove the instances where the setup had drifted and the optical heterodyne detection efficiency was compromised. The same histogram after removing such points is shown in panel B.

## C. Frequency Domain Analysis

As already mentioned in the main text, with the help of time-domain analysis, we select three different time-snippets to analyze the data in the frequency domain - before-pulse, in-pulse and after-pulse defined with respect to the first optical pump pulse. The main challenge in processing the data in the frequency domain is the proper normalization of the measured output spectrum [cf. Eq. S48]. The microwave reflection baseline is not flat because of slight impedance mismatches between different components in the microwave detection chain. Similarly, the optical heterodyne shot noise floor is also not flat due to the frequency dependent balanced detector gain. In addition, we observe small offsets of a few millivolts in the digitizer noise levels each time a new measurement is launched and the digitizer is reinitialized. Combined with the fact that the amplifier gain in the microwave detection chain as well as the optical heterodyne gain (due to optical LO power drift) may drift over a long time scales, an in-situ calibration of vacuum noise level is needed.

In case of microwave measurements, we need to first correct for the microwave reflection baseline distortion from impedance mismatch and then correct for the signal level shift caused by the digitizer. For the distorted baseline, we

separately measure the microwave output spectrum when the microwave cavity is in its ground state (thermalized to 7 mK at the mixing chamber, laser off). This cold measurement is done exactly the same way as the downconversion measurements except with a much faster repetition rate to save time. It is shown in Fig S5A (gray) along with the measured (and not normalized) before-pulse (cyan), in-pulse (purple) and after-pulse microwave noise spectrum (orange). Dividing the measured spectra with the cold cavity spectrum reveals a flat baseline Lorentzian noise spectra shown in the main text, however with an offset due to reinitialization of the digitizer for each measurement. To correct for this offset, we perform an in-situ vacuum noise calibration using the measured off-resonant (waveguide) noise baseline in the before-pulse microwave noise spectrum.

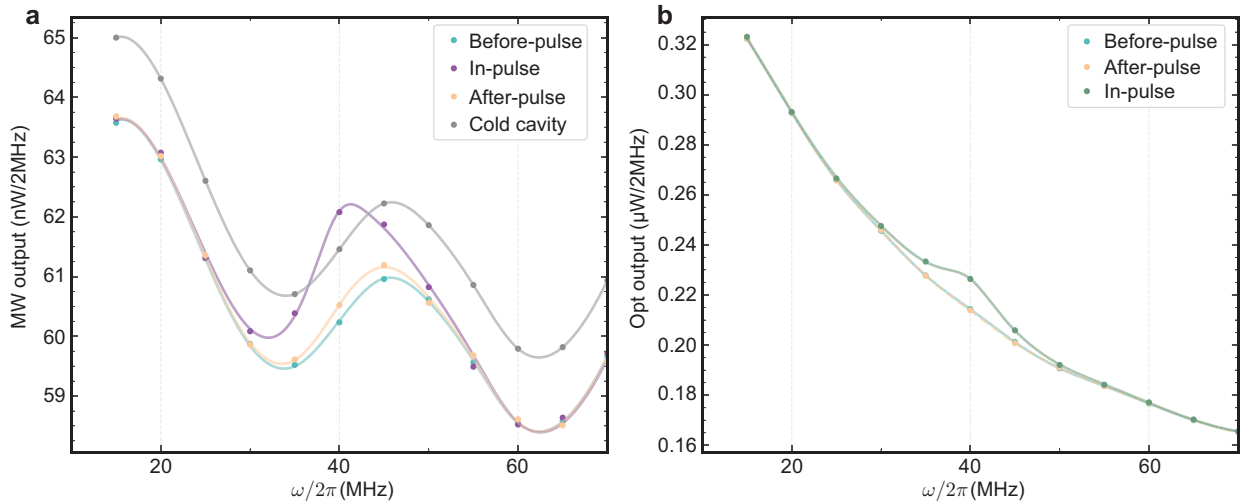


Figure S8. **Measured output power spectral densities.** **A**, the measured raw microwave output power spectrum for four different time regions, as indicated in the legend. The cold cavity baseline (no laser light) has an extra offset with respect to all other measurements due to digitizer offsets which is corrected with an in-situ reference measurement. Panel **B** shows the output spectra for the optical output before (during, after) the first optical pulse in cyan (green, orange).

In the following we present supporting data that shows that this reference measurement indeed probes the equivalent shot-noise level with the waveguide initialized in its quantum ground state. In our previous work Ref. (14) we showed that the microwave bath noise is consistent for a given time-averaged pump power. This allows us to back out the absolute waveguide noise for each average optical pump power based on a more reliable and efficient measurement.

Here we measure the off-resonant waveguide noise continuously and averaged over the full duty cycle with a spectrum analyzer, which offers smaller measurement drifts, as a function of optical pump power shown in Fig S9. The error bars of individual data points are still significant with a  $2\sigma$ -error  $\sim 0.04$  photons, mostly due to remaining drifts in the measurement device. The power law fit between waveguide noise and average optical pump power reveals that the microwave waveguide noise grows approximately linearly with average optical pump power, and only deviates clearly from 0 for optical pump power  $> 3 \mu\text{W}$ . We extrapolate the waveguide noise for the average pump power that we work with  $\sim 0.1 \mu\text{W}$  from the fit (marked with 'X') and find the value of the fit to be  $(0.001 \pm 0.002)$ . This number which is also reported in the main text is so small because it corresponds to the fit error and not the uncertainty corresponding to the individual measured data point.

This power dependent measurement provides strong evidence that the waveguide spectrum is very well thermalized when slow repetition rates are used that result in a low average optical pump power of only  $\sim 0.1 \mu\text{W}$ . The off-resonant noise measured right before the optical pulse in the microwave noise spectrum therefore serves as a valid in-situ vacuum noise calibration. In Tab. S2, we list the on-resonance and the off-resonance (waveguide) output microwave noise for all the three different time-snippets: before-, in- and after-pulse.

Table S2. Fit output microwave noise on-resonance and off-resonance (waveguide noise) for the three different analyzed time-snippets with  $2\sigma$  errors.

	Before-pulse	In-pulse	After-pulse
On-resonance noise	$(0.026 \pm 0.022)$	$(0.458 \pm 0.097)$	$(0.087 \pm 0.066)$
Waveguide noise	$(-0.002 \pm 0.019)$	$(-0.019 \pm 0.045)$	$(0.000 \pm 0.034)$

In case of optics, the optical detection is shot-noise limited, and the excess LO noise at the optical signal frequency

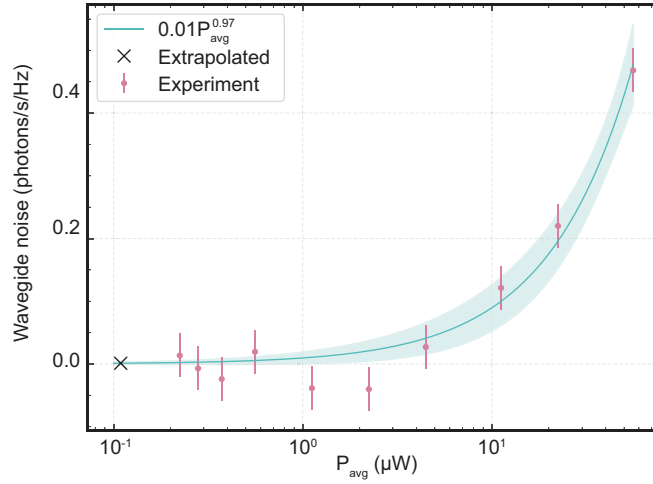


Figure S9. **Microwave waveguide noise as a function of average optical pump power.** Here we swept the pulse repetition time from 500 ms to 2 ms. The error bars represent the  $2\sigma$  error. The solid line is a power law fit with exponent 0.97. The shaded area represents the  $2\sigma$ -error of the fit. 'X' marks the average optical pump power we used in the main text. Extrapolating the fit to this mark gives us the waveguide noise mentioned in the main text.

is suppressed by more than 40 dB using filter F1 shown in Fig. S1. We use the before-pulse optical noise spectrum as the vacuum noise level and normalize the optical in-pulse spectrum directly with the before-pulse in-situ calibration. Fig. S8b shows the noise spectrum (without normalization) of the optical before-pulse (cyan), in-pulse (green), and the after-pulse (yellow). The signal during the optical pump pulse is clearly visible, and the noise level is identical before and after the optical pulse.

The normalized noise spectra for both microwave and optics are shown in main text Fig. 2d and 2e., where we can obtain the normalization gain [cf. Eq. S48].

#### D. Joint-quadrature Correlations

The detected output quadratures including excess added noise, i.e.  $\hat{I}_{X_e, \text{out}}(\Delta\omega)$ ,  $\hat{I}_{P_e, \text{out}}(\Delta\omega)$ ,  $\hat{I}_{X_o, \text{out}}(\Delta\omega)$ ,  $\hat{I}_{P_o, \text{out}}(\Delta\omega)$ , can be obtained from the real and imaginary parts in the discrete Fourier transform of the photocurrent by normalizing to the detection gain [cf. Eq. S50].

Similar to Sec. IC1, we can define the joint detected quadratures, by applying phase rotation on the optical ones,

$$\begin{aligned}\hat{I}_{X,+}(\Delta\omega, \phi) &= \frac{\hat{I}_{X_e, \text{out}}(\Delta\omega) + [\hat{I}_{X_o, \text{out}}(\Delta\omega) \cos \phi - \hat{I}_{P_o, \text{out}}(\Delta\omega) \sin \phi]}{\sqrt{2}}, \\ \hat{I}_{P,-}(\Delta\omega, \phi) &= \frac{\hat{I}_{P_e, \text{out}}(\Delta\omega) - [\hat{I}_{X_o, \text{out}}(\Delta\omega) \sin \phi + \hat{I}_{P_o, \text{out}}(\Delta\omega) \cos \phi]}{\sqrt{2}}.\end{aligned}\tag{S71}$$

To verify the non-classical correlation between the unitless quadrature variables for output microwave and optics field, i.e.  $\hat{X}_e(\Delta\omega)$  &  $\hat{X}_o(-\Delta\omega)$  and  $\hat{P}_e(\Delta\omega)$  &  $\hat{P}_o(-\Delta\omega)$ , we can calculate the phase dependent joint quadrature variance [cf. Eq. S61],

$$\begin{aligned}\langle \hat{X}_+^2(\Delta\omega, \phi) \rangle &= \langle \hat{I}_{X,+}^2(\Delta\omega, \phi) \rangle - \frac{N_{e, \text{add}} + N_{o, \text{add}}}{2}, \\ \langle \hat{P}_-^2(\Delta\omega, \phi) \rangle &= \langle \hat{I}_{P,-}^2(\Delta\omega, \phi) \rangle - \frac{N_{e, \text{add}} + N_{o, \text{add}}}{2}.\end{aligned}\tag{S72}$$

For  $\Delta\omega = 0$ , we plot the joint quadrature variance as a function of local oscillator phase in Fig. S10 (a). The shaded region represent the  $2\sigma$  statistical error in the calculated joint quadrature variances. We note that, the statistical  $1\sigma$  error of the variance for a Gaussian distributed data is given by  $\sqrt{2}\sigma^2/\sqrt{N-1}$ , where  $N$  is the length of the dataset. The obtained resonant  $\Delta_{\text{EPR}}(0, \phi)$  is shown in Fig. S10B. The minimum and maximum of  $\Delta_{\text{EPR}}(\phi)$  over the local

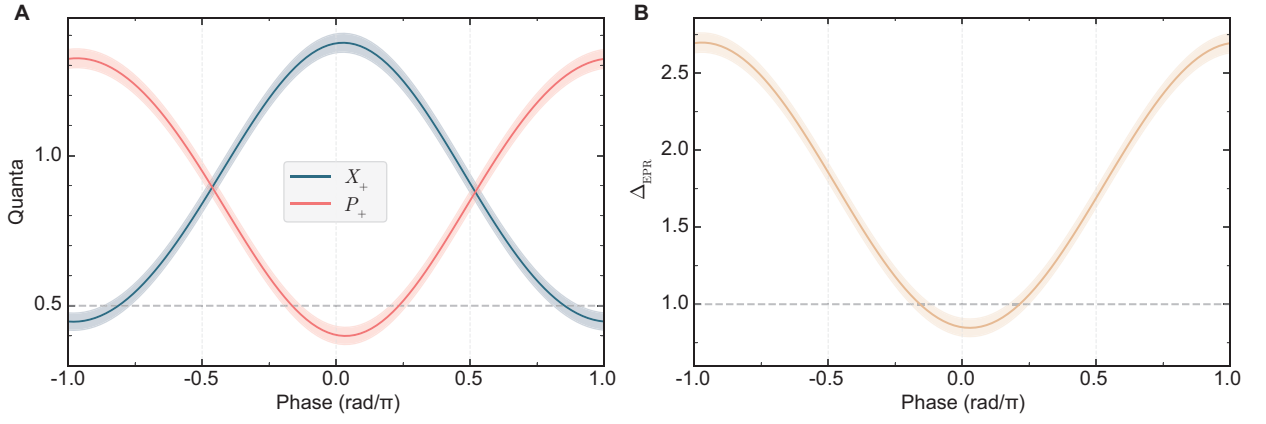


Figure S10. **Joint quadrature correlations and  $\Delta_{\text{EPR}}$ .** (A) Joint quadratures at resonance  $X_+(\Delta\omega = 0)$  and  $P_+(\Delta\omega = 0)$  are plotted as a function of the local oscillator phase  $\phi$ . (B)  $\Delta_{\text{EPR}}$  as a function of  $\phi$ . The shaded region in both plots represents the  $2\sigma$  statistical error.

oscillator phase are defined as  $\min[\Delta_{\text{EPR}}] = \Delta_{\text{EPR}}^-$  and  $\max[\Delta_{\text{EPR}}] = \Delta_{\text{EPR}}^+$ .  $\Delta_{\text{EPR}}^- < 1$  indicates non-classical joint correlations and squeezing below vacuum levels.

The broadband phase that minimizes  $\Delta_{\text{EPR}}(\Delta\omega, \phi)$ , i.e.  $\phi_{\min}(\Delta\omega)$ , reveals the difference in arrival times (group delay) between the microwave and optical signal output (Fig. S11A). After fixing the inferred time delay between the in-pulse arrival time of the microwave and optical signal,  $\phi_{\min}$  becomes independent of frequency detuning from the mode resonances. Thus, we adjust for the differences in arrival times by ensuring that the slope of  $\phi_{\min}$  with respect to detuning  $\Delta\omega$  is minimized for all datasets we analyze, utilizing the broadband quantum correlations.

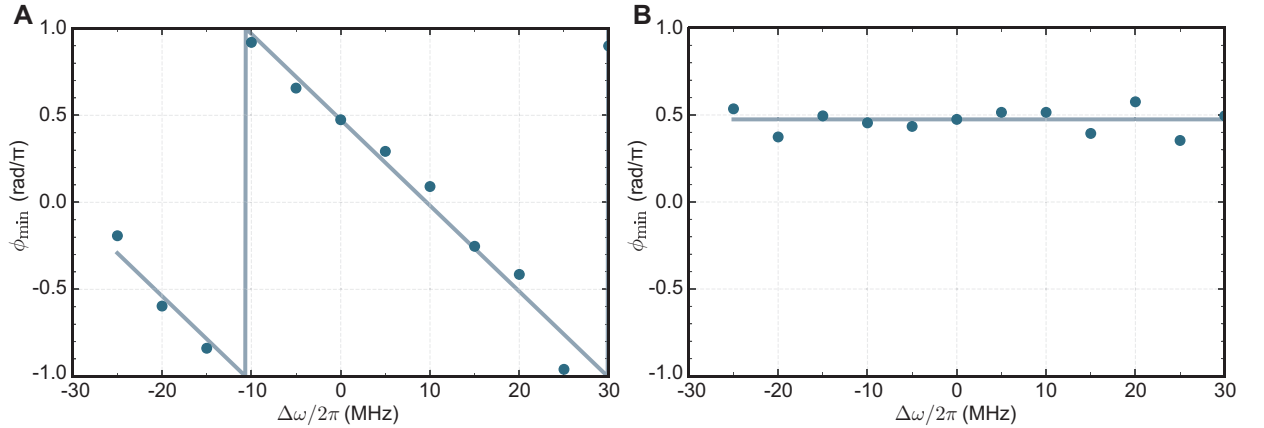


Figure S11. **Effect of time delay between the microwave and optics signals.** The plots show the local oscillator phase  $\phi_{\min}$  which minimizes  $\Delta_{\text{EPR}}(\Delta\omega, \phi)$  as a function of detuning frequency  $\Delta\omega$ . (A and B) shows the case when the time difference of arrival between the microwave and optics signals was 25 ns and  $\approx 0$  ns respectively. The solid lines are the linear fit to the experimental data.

## V. QUADRATURE HISTOGRAM RAW DATA

Fig. S12 shows the normalized difference of the two-variable quadrature histograms obtained during and before the optical pump pulse based on the data shown in Figs. 2 and 3 of main text. These unprocessed histograms directly show the phase insensitive amplification in each channel as well as the correlations in  $(X_e, X_o)$  and  $(P_e, P_o)$ . Note however that - in contrast to the analysis in the main text - taking this difference does not lead to a valid phase space representation since also the vacuum noise of 0.5 together with the output noise of  $0.026 \pm 0.011$  photons (due to the residual microwave bath occupancy right before the pulse) are subtracted, hence the negative values.

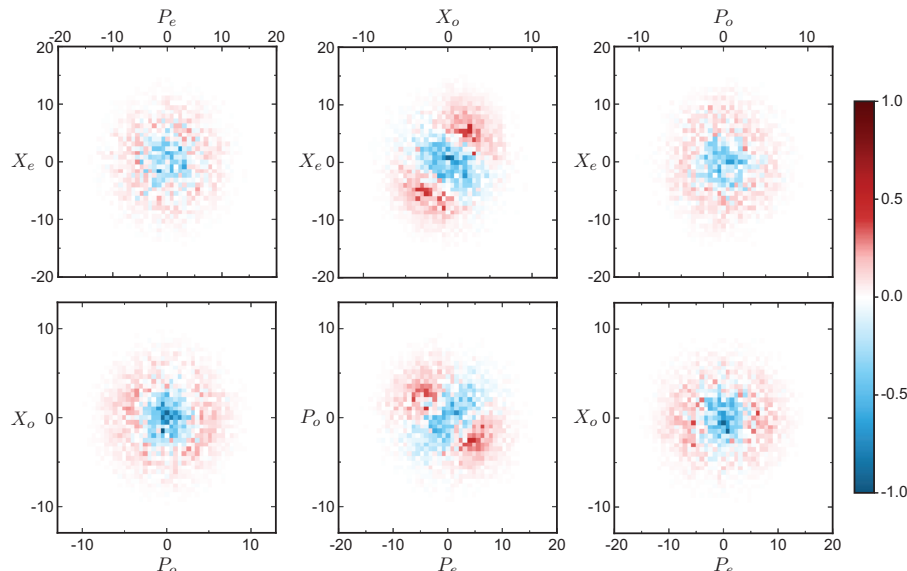


Figure S12. **Quadrature histogram raw data.** Normalized difference of the two-variable quadrature histograms obtained during and before the optical pump pulse based on the data shown in Figs. 2 and 3 of the main text.

## VI. NON-CLASSICAL CORRELATIONS WITH 600 ns LONG OPTICAL PUMP PULSES

Before experimenting with 250 ns long optical pump pulses, we used 600 ns long optical pump pulses. A sample measurement with a 600 ns is shown in Fig. S13A similar to Fig. 3C of main text. Compared to 250 ns long pulses, the main difference lies in the fact that  $\Delta_{\text{EPR}}^-$  in the middle panel exhibits a double-dip shape because the correlations  $\bar{V}_{13}$  have a wider bandwidth than the emitted noise spectra ( $\bar{V}_{11}$  and  $\bar{V}_{33}$ ), which are narrowed due to dynamical back-action (28). Since in the measurement the correlations don't clearly overwhelm the emitted noise, interference between two Lorentzian functions of different widths (dashed line) leads to the specific shape of  $\Delta_{\text{EPR}}^-$ . Theory confirms this even though the shown theory curve (solid red line) does not exhibit the specific line-shape due to higher expected correlations compared to the experimentally observed values. These results indicate that  $\bar{n}_{e,\text{int}}$  due to a 600 ns optical pump pulse is large enough to prevent a clear observation of squeezing over the full bandwidth below the vacuum level ( $\Delta_{\text{EPR}}^- < 1$ ). As a result, we switched to 250 ns optical pump pulses with higher statistics as shown in the main text.

We also repeated the measurement with 600 ns long pulses with different optical pump powers. Fig. S13B shows the measured pump power dependence with each data point based on 170000-412500 individual measurements each with a 2 Hz repetition rate. The microwave mode thermal bath occupancy  $\bar{n}_{e,\text{int}}$  changes little as a function of the peak optical pump power at the device and is approximated with a constant function (solid maroon line in the top panel). The on-resonance mean CM elements scale with cooperativity and are in excellent agreement with theory (solid lines) based on the  $\bar{n}_{e,\text{int}}$ . The *on-resonance* squeezing  $\Delta_{\text{EPR}}^-$  does not change significantly with cooperativity since both excess noise and correlations scale together with cooperativity. The anti-squeezing  $\Delta_{\text{EPR}}^+$  scales up with cooperativity as expected. All but one measured mean values are below the vacuum level and three power settings show a  $> 2\sigma$  significance for entanglement. Note that this power sweep was conducted on a different set of optical modes with a different amount of anti-Stokes sideband suppression (see section III).

## VII. ERROR ANALYSIS

The covariance matrix of the output field quadratures  $V(\omega)$  can be directly calculated from the extracted microwave and optical quadratures from frequency domain analysis [cf. Eq. S54]. We simply rotate the optical quadratures with the phase that minimized the joint quadrature variance, and obtain the covariance matrix in the normal form. We note that, the error in calculating the covariance matrix comes from two sources - the statistical error due to finite number of pulses, and the systematic error in the vacuum noise level calibration. The detailed error analysis is described in the following subsections. We note that, *the uncertainty in all the reported numbers in the main text corresponds to 2 standard deviation.*

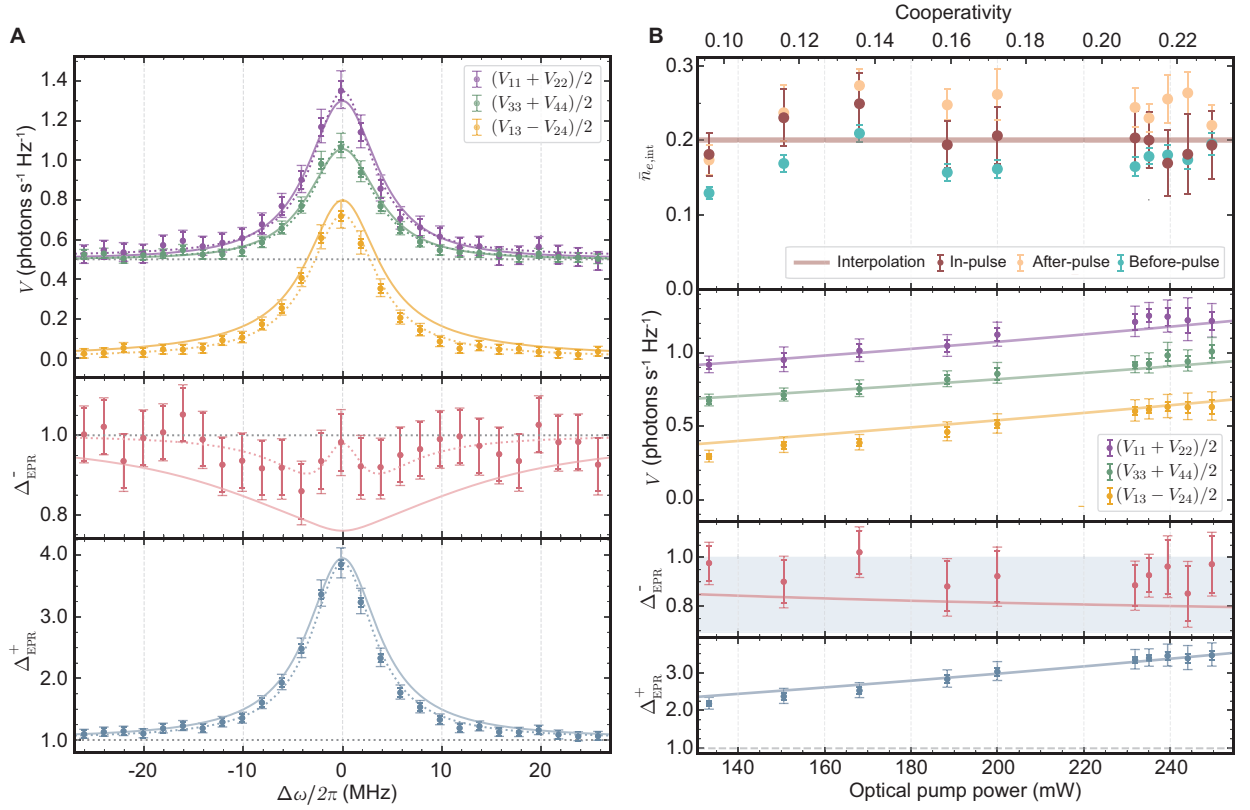


Figure S13. **Non-classical correlations vs. optical pump power for 600 ns long pump pulses.** **A**, Top panel, the average microwave output noise  $\bar{V}_{11}$  (purple), the optical output noise  $\bar{V}_{33}$  (green) and correlations  $\bar{V}_{13}$  (yellow) as a function detuning based on 412500 measurements with a 2 Hz repetition rate. The solid lines represent the joint theory with fit parameters  $C = 0.22$  and in-pulse microwave thermal bath occupancy  $\bar{n}_{e,int} = 0.19 \pm 0.03$ . The dashed lines are individual Lorentzian fits to serve as a guide to the eye.  $\Delta_{EPR}^-$  ( $\Delta_{EPR}^+$ ) in the middle (bottom) panel shown in red (blue) color are calculated from the top panel data and fits as described in the main text. The darker color error bars represent the  $2\sigma$  statistical error and the outer (faint) error bars also include systematic errors. **B**, Power dependence of CM elements. The top panel shows the microwave mode thermal bath occupancy  $\bar{n}_{e,int}$  for before-pulse, after-pulse and in-pulse regimes (marked in Fig. 2A) as a function of the peak optical pump power at the device and the corresponding cooperativity. The in-pulse  $\bar{n}_{e,int}$  is obtained by the joint theory fit and approximated with a constant function (solid line). The middle panel shows the on-resonance mean CM elements based on the  $\bar{n}_{e,int}$  from the top panel. The bottom two panels show the *on-resonance* squeezing  $\Delta_{EPR}^-$  and anti-squeezing  $\Delta_{EPR}^+$  calculated from the middle panel along with theory (solid lines). The darker color error bars represent the  $2\sigma$  statistical error and the outer (faint) error bars also include systematic errors. All measured mean values are below the vacuum level and three power settings show a  $> 2\sigma$  significance for entanglement.

### A. Statistical Error

The error in the calculation of bivariate variances comes from the statistical uncertainties, arising from finite number of observations of a random sample. This error is the major component of our total error in diagonal covariance matrix elements. The error in calculating the variance of a sample distribution sampled from a Gaussian variable follows the Chi-squared distribution and is given as,

$$\text{Var}(\sigma^2) = \frac{2\sigma^2}{N-1}, \quad (\text{S73})$$

where,  $\sigma^2$  is the variance of sample distribution and  $N$  is its size.

In addition, the error in the covariance from a bivariate variable is given by the Wishart distribution (52). For a general bivariate covariance matrix  $\Sigma$  given as,

$$\Sigma = \begin{pmatrix} \sigma_{11}^2 & \rho\sigma_{11}\sigma_{22} \\ \rho\sigma_{11}\sigma_{22} & \sigma_{22}^2 \end{pmatrix}, \quad (\text{S74})$$



the variance of the covariance matrix is given by,

$$\text{Var}(\Sigma) = \frac{1}{N-1} \begin{pmatrix} 2\sigma_{11}^4 & (1+\rho^2)\sigma_{11}^2\sigma_{22}^2 \\ (1+\rho^2)\sigma_{11}^2\sigma_{22}^2 & 2\sigma_{22}^4 \end{pmatrix}. \quad (\text{S75})$$

### B. Systematic Error

Although, the systematic error in our measurements are not as significant, they still are a noticeable source of error. Here the error in calculating the covariance matrix results from the error in the estimation of the vacuum noise levels. More specifically, the error in determining the added noise due to the microwave and optical detection chain, as discussed in Sec. III. Propagating these systematic errors through the covariance matrix analysis is non-trivial, since calculating the error in variance of erroneous quantities is challenging. Therefore, we use a worst-case scenario approach to calculate the total error including the statistical error and the systematic error. We repeat the full analysis, including the statistical errors, for the lower and upper bound of the uncertainty range from the systematic errors for the microwave and optical added noise levels. Repeating the analysis expands the error bars in the calculated quantities. We take the extremum of all the error bars from all the repetitions of analysis to get the total error bar. We show both statistical error and the total error in the main text.

## VIII. ENTANGLEMENT FIGURES OF MERIT

### Rate of entanglement generation

From the log negativity  $E_N$  (Eq. S64), we can calculate the formation of entanglement  $E_f$  (54),

$$E_f = \sigma_+ \log_2 \sigma_+ - \sigma_- \log_2 \sigma_-, \quad (\text{S76})$$

where  $\sigma_{\pm} = (1/\sqrt{\theta} \pm \sqrt{\theta})^2/4$  with  $\theta = 2^{-E_N}$ . With  $E_N = 0.17$ , for the two-mode squeezed state that we generate, we find  $E_f = 0.035$  ebit/s/Hz. Integrating this over the emission bandwidth of  $\approx 10$  MHz and the measured pulse length of 200 ns, we find the total  $E_f$  generated over one optical pump pulse to be about 0.11 ebits per pulse. Since our repetition rate is only 2 Hz, we produce about 0.22 ebit/s. This rate can be significantly increased with higher pulse repetition rates which are limited by high optical peak power in each pulse. With a ten-fold improvement in optical quality factors alone, we can reduce the optical pump power needed by about 100 times, thus reducing the thermal load on our device significantly and allowing for much faster repetition rates.

### Squeezing improvements

In this following, we explore various figures of merit of the two-mode squeezed state produced from an electrooptic device as a function of the two main device parameters - coupling efficiencies to the cavities and the cooperativity. Since the device is symmetric between the two cavities - microwave and optics, we calculate various quantities as a function of  $\eta_i = \eta_e = \eta_o$ . Moreover, here we only report the two-mode squeezed state produced at cavity resonance ( $\Delta\omega = 0$ ) with the microwave mode at the thermal occupation  $\bar{n}_{e,\text{int}} = 0.1$ , which is the upper limit of what we measured experimentally.

Figure S14(A) shows the squeezing  $\Delta_{\text{EPR}}^-$  as a function of  $\eta_i$  and  $C$ . As expected, the squeezing increases, i.e.  $\Delta_{\text{EPR}}^-$  approaches zero, with increasing cooperativity and coupling efficiencies, and one can see that the latter is more relevant to achieve values close to zero. In principle it is possible to achieve an arbitrary amount of squeezing with this system if  $\eta_i, C \rightarrow 1$  irrespective of the microwave intrinsic thermal occupancy  $\bar{n}_{e,\text{int}}$ .

We also calculate the effective squeezing parameter  $r$  obtained from an effective thermal two-mode squeezer model Eq. S68.  $r$  increases as expected as a function of increasing  $\eta_i$  and  $C$  as shown in Fig. S14(B).

In Fig. S14(C), we plot the state purity  $\rho = 1/(4\sqrt{\det[V]})$  for different device parameters. The purity is 1 at  $C \sim 0$  because we only couple out vacuum which has  $\rho = 1$ . This is because we assume the waveguide noise photon number to be 0 for these calculation.  $\rho$  generally decreases as a function of  $C$  because the correlations produced ( $V_{13}$ ) are always slightly lower than the thermal noise amplified from vacuum ( $V_{11}, V_{33}$ ) making the  $\det[V]$  large as all the CM elements increase with  $C$ . This is also true for the ideal case of  $\bar{n}_{e,\text{int}} = 0$ . We find  $\rho = 1$  for all cooperativities when  $\eta_i = 1$ , even though it's not clearly visible in the plot.



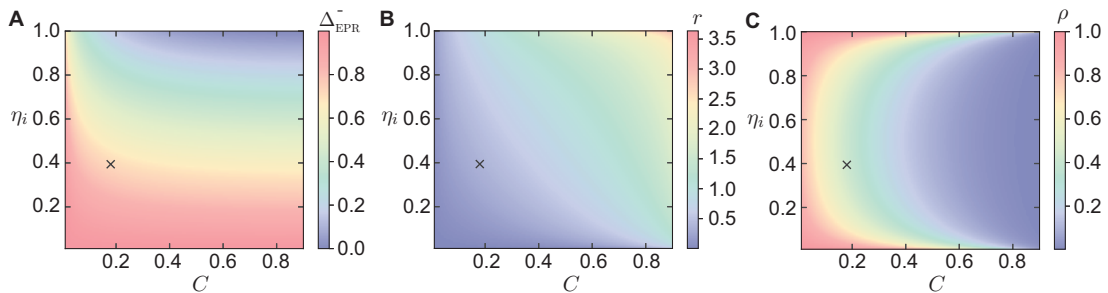


Figure S14. **Entanglement figures of merit as a function of device parameters.** Calculated  $\Delta_{\text{EPR}}^-$  (A), effective squeezing  $r$  (B) and state purity  $\rho$  (C) as a function of coupling efficiency  $\eta_o = \eta_e = \eta_i$  and cooperativity  $C$  for a microwave thermal occupancy  $\bar{n}_{e,\text{int}} = 0.1$ . The grey crosses mark the current device parameters.

## IX. FUTURE APPLICATIONS

### Quantum state transfer

In the introduction of the main manuscript, we motivate the generation of microwave-optics entanglement with deterministic state transfer. Deterministic transfer of a nonclassical state using direct microwave to optics conversion requires  $> 50\%$  total efficiencies even when no extra noise is added in the process. As a result, direct conversion has a certain threshold below which deterministic state transfer is not possible (see Fig. 2 of Ref (22)). In contrast, using entanglement in teleportation-based schemes which are assisted by a reliable classical communication channel, the state transfer fidelities are always finite. In other words, the quantum capacity of the teleportation-based channel is never zero, no matter how small the shared entanglement is.

From Refs. (21, 22) which compare state transfer fidelities between a teleportation-based channel versus a direct transduction channel for an electrooptic transducer, we find that for our current device parameters quantum state transfer fidelities of  $\sim 50-60\%$  for a squeezed input state is possible compared to  $< 10\%$  fidelity for direct transduction of the same state.

If on the other hand this same device and experiment is used for quantum state transfer via teleportation in the more loss resilient discrete variable domain via single photon counting measurements, the amount of squeezing is not the main concern. In fact, one would need to work at lower pump powers to avoid multi-photon generation events in order to reliably stay in the 0-1 logical basis. We conclude that this device is also very much suitable for the photon counting approach and the most important improvements concern better out-coupling efficiency (lower internal losses) as well as a higher repetition rate (lower pump power, shorter pulses, better thermalization).

### Entanglement distribution from CV entangled states to qubits

In the present paper we generate entanglement between two propagating radiation fields in the continuous variable domain. Ref. (38) explores how such a state can be used to distribute this entanglement to discrete variable qubits (two-level systems) by directly driving them with the generated two-mode-squeezed state. In this case, the fidelity of distributed qubit entanglement  $\mathcal{F}$  (defined as the overlap with the ideal Bell state) can be characterized by the state purity  $\rho$  and the effective squeezing  $r$  of the state generated by the entanglement source.

We calculate this fidelity of generated qubit entanglement  $\mathcal{F}$  as a function of system parameters - coupling efficiency and cooperativity - as shown in Fig. S15. The two qubits are entangled if  $\mathcal{F} > 0.5$  which is marked by a solid line. The grey cross represents the current device parameters which corresponds to about 35% entanglement fidelity of the two qubits. However, with reasonable improvements to our device ( $\eta_i \sim 0.7$  and lower  $C$ ), finite remote qubit entanglement  $\mathcal{F} > 0.5$  can be generated.

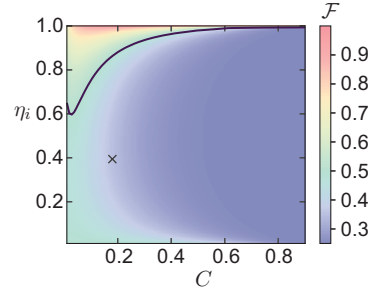


Figure S15. **Distributed qubit entanglement fidelity.** Calculated fidelity of distributed entanglement  $\mathcal{F}$  of two qubits that are driven by a two-mode squeezed state generated by a device with parameters  $\eta_i = \eta_e = \eta_o$  and  $C$  and microwave thermal occupancy  $\bar{n}_{e,\text{int}} = 0.1$ . The solid lines marks the contour  $\mathcal{F} = 0.5$  above which qubits are entangled. The grey cross marks the current device parameters.

## References and Notes

1. F. Arute, K. Arya, R. Babbush, D. Bacon, J. C. Bardin, R. Barends, R. Biswas, S. Boixo, F. G. S. L. Brandao, D. A. Buell, B. Burkett, Y. Chen, Z. Chen, B. Chiaro, R. Collins, W. Courtney, A. Dunsworth, E. Farhi, B. Foxen, A. Fowler, C. Gidney, M. Giustina, R. Graff, K. Guerin, S. Habegger, M. P. Harrigan, M. J. Hartmann, A. Ho, M. Hoffmann, T. Huang, T. S. Humble, S. V. Isakov, E. Jeffrey, Z. Jiang, D. Kafri, K. Kechedzhi, J. Kelly, P. V. Klimov, S. Knysh, A. Korotkov, F. Kostritsa, D. Landhuis, M. Lindmark, E. Lucero, D. Lyakh, S. Mandrà, J. R. McClean, M. McEwen, A. Megrant, X. Mi, K. Michielsen, M. Mohseni, J. Mutus, O. Naaman, M. Neeley, C. Neill, M. Y. Niu, E. Ostby, A. Petukhov, J. C. Platt, C. Quintana, E. G. Rieffel, P. Roushan, N. C. Rubin, D. Sank, K. J. Satzinger, V. Smelyanskiy, K. J. Sung, M. D. Trevithick, A. Vainsencher, B. Villalonga, T. White, Z. J. Yao, P. Yeh, A. Zalcman, H. Neven, J. M. Martinis, Quantum supremacy using a programmable superconducting processor. *Nature* **574**, 505–510 (2019). [doi:10.1038/s41586-019-1666-5](https://doi.org/10.1038/s41586-019-1666-5) [Medline](#)
2. M. Zhong, M. P. Hedges, R. L. Ahlefeldt, J. G. Bartholomew, S. E. Beavan, S. M. Wittig, J. J. Longdell, M. J. Sellars, Optically addressable nuclear spins in a solid with a six-hour coherence time. *Nature* **517**, 177–180 (2015). [doi:10.1038/nature14025](https://doi.org/10.1038/nature14025) [Medline](#)
3. Y. Yu, F. Ma, X.-Y. Luo, B. Jing, P.-F. Sun, R.-Z. Fang, C.-W. Yang, H. Liu, M.-Y. Zheng, X.-P. Xie, W.-J. Zhang, L.-X. You, Z. Wang, T.-Y. Chen, Q. Zhang, X.-H. Bao, J.-W. Pan, Entanglement of two quantum memories via fibres over dozens of kilometres. *Nature* **578**, 240–245 (2020). [doi:10.1038/s41586-020-1976-7](https://doi.org/10.1038/s41586-020-1976-7) [Medline](#)
4. Z.-L. Xiang, S. Ashhab, J. Q. You, F. Nori, Hybrid quantum circuits: Superconducting circuits interacting with other quantum systems. *Rev. Mod. Phys.* **85**, 623–653 (2013). [doi:10.1103/RevModPhys.85.623](https://doi.org/10.1103/RevModPhys.85.623)
5. G. Kurizki, P. Bertet, Y. Kubo, K. Mølmer, D. Petrosyan, P. Rabl, J. Schmiedmayer, Quantum technologies with hybrid systems. *Proc. Natl. Acad. Sci. U.S.A.* **112**, 3866–3873 (2015). [doi:10.1073/pnas.1419326112](https://doi.org/10.1073/pnas.1419326112) [Medline](#)
6. A. A. Clerk, K. W. Lehnert, P. Bertet, J. R. Petta, Y. Nakamura, Hybrid quantum systems with circuit quantum electrodynamics. *Nat. Phys.* **16**, 257–267 (2020). [doi:10.1038/s41567-020-0797-9](https://doi.org/10.1038/s41567-020-0797-9)
7. L.-M. Duan, M. D. Lukin, J. I. Cirac, P. Zoller, Long-distance quantum communication with atomic ensembles and linear optics. *Nature* **414**, 413–418 (2001). [doi:10.1038/35106500](https://doi.org/10.1038/35106500) [Medline](#)
8. S.-H. Wei, B. Jing, X.-Y. Zhang, J.-Y. Liao, C.-Z. Yuan, B.-Y. Fan, C. Lyu, D.-L. Zhou, Y. Wang, G.-W. Deng, H.-Z. Song, D. Oblak, G.-C. Guo, Q. Zhou, Towards real-world quantum networks: A review. *Laser Photonics Rev.* **16**, 2100219 (2022). [doi:10.1002/lpor.202100219](https://doi.org/10.1002/lpor.202100219)
9. G. Burkard, T. D. Ladd, J. M. Nichol, A. Pan, J. R. Petta, Semiconductor spin qubits. [arXiv:2112.08863](https://arxiv.org/abs/2112.08863) [cond-mat.mes-hall] (2021).
10. P. Magnard, S. Storz, P. Kurpiers, J. Schär, F. Marxer, J. Lütolf, T. Walter, J.-C. Besse, M. Gabureac, K. Reuer, A. Akin, B. Royer, A. Blais, A. Wallraff, Microwave quantum link

- between superconducting circuits housed in spatially separated cryogenic systems. *Phys. Rev. Lett.* **125**, 260502 (2020). [doi:10.1103/PhysRevLett.125.260502](https://doi.org/10.1103/PhysRevLett.125.260502) [Medline](#)
11. Y. Zhong, H.-S. Chang, A. Bienfait, É. Dumur, M.-H. Chou, C. R. Conner, J. Grebel, R. G. Povey, H. Yan, D. I. Schuster, A. N. Cleland, Deterministic multi-qubit entanglement in a quantum network. *Nature* **590**, 571–575 (2021). [doi:10.1038/s41586-021-03288-7](https://doi.org/10.1038/s41586-021-03288-7) [Medline](#)
  12. X. Han, W. Fu, C.-L. Zou, L. Jiang, H. X. Tang, Microwave-optical quantum frequency conversion. *Optica* **8**, 1050 (2021). [doi:10.1364/OPTICA.425414](https://doi.org/10.1364/OPTICA.425414)
  13. M. Mirhosseini, A. Sipahigil, M. Kalaei, O. Painter, Superconducting qubit to optical photon transduction. *Nature* **588**, 599–603 (2020). [doi:10.1038/s41586-020-3038-6](https://doi.org/10.1038/s41586-020-3038-6) [Medline](#)
  14. R. Sahu, W. Hease, A. Rueda, G. Arnold, L. Qiu, J. M. Fink, Quantum-enabled operation of a microwave-optical interface. *Nat. Commun.* **13**, 1276 (2022). [doi:10.1038/s41467-022-28924-2](https://doi.org/10.1038/s41467-022-28924-2) [Medline](#)
  15. B. M. Brubaker, J. M. Kindem, M. D. Urmey, S. Mittal, R. D. Delaney, P. S. Burns, M. R. Vissers, K. W. Lehnert, C. A. Regal, Optomechanical Ground-State Cooling in a Continuous and Efficient Electro-Optic Transducer. *Phys. Rev. X* **12**, 021062 (2022). [doi:10.1103/PhysRevX.12.021062](https://doi.org/10.1103/PhysRevX.12.021062)
  16. A. Kumar, A. Suleymanzade, M. Stone, L. Taneja, A. Anferov, D. I. Schuster, J. Simon, Quantum-enabled millimetre wave to optical transduction using neutral atoms. *Nature* **615**, 614–619 (2023). [doi:10.1038/s41586-023-05740-2](https://doi.org/10.1038/s41586-023-05740-2) [Medline](#)
  17. M. J. Weaver, P. Duivestijn, A. C. Bernasconi, S. Scharmer, M. Lemang, T. C. van Thiel, F. Hijazi, B. Hensen, S. Gröblacher, R. Stockill, An integrated microwave-to-optics interface for scalable quantum computing. [arXiv:2210.15702](https://arxiv.org/abs/2210.15702) [quant-ph] (2022).
  18. S. Takeda, T. Mizuta, M. Fuwa, P. van Loock, A. Furusawa, Deterministic quantum teleportation of photonic quantum bits by a hybrid technique. *Nature* **500**, 315–318 (2013). [doi:10.1038/nature12366](https://doi.org/10.1038/nature12366) [Medline](#)
  19. K. G. Fedorov, M. Renger, S. Pogorzalek, R. Di Candia, Q. Chen, Y. Nojiri, K. Inomata, Y. Nakamura, M. Partanen, A. Marx, R. Gross, F. Deppe, Experimental quantum teleportation of propagating microwaves. *Sci. Adv.* **7**, eabk0891 (2021). [doi:10.1126/sciadv.abk0891](https://doi.org/10.1126/sciadv.abk0891) [Medline](#)
  20. S. L. N. Hermans, M. Pompili, H. K. C. Beukers, S. Baier, J. Borregaard, R. Hanson, Qubit teleportation between non-neighbouring nodes in a quantum network. *Nature* **605**, 663–668 (2022). [doi:10.1038/s41586-022-04697-y](https://doi.org/10.1038/s41586-022-04697-y) [Medline](#)
  21. A. Rueda, W. Hease, S. Barzanjeh, J. M. Fink, Electro-optic entanglement source for microwave to telecom quantum state transfer. *npj Quantum Inf.* **5**, 108 (2019).
  22. J. Wu, C. Cui, L. Fan, Q. Zhuang, Deterministic microwave-optical transduction based on quantum teleportation. *Phys. Rev. Appl.* **16**, 064044 (2021). [doi:10.1103/PhysRevApplied.16.064044](https://doi.org/10.1103/PhysRevApplied.16.064044)
  23. U. L. Andersen, T. Gehring, C. Marquardt, G. Leuchs, 30 years of squeezed light generation. *Phys. Scr.* **91**, 053001 (2016). [doi:10.1088/0031-8949/91/5/053001](https://doi.org/10.1088/0031-8949/91/5/053001)

24. W. Hease, A. Rueda, R. Sahu, M. Wulf, G. Arnold, H. G. L. Schwefel, J. M. Fink, Bidirectional electro-optic wavelength conversion in the quantum ground state. *PRX Quantum* **1**, 020315 (2020). [doi:10.1103/PRXQuantum.1.020315](https://doi.org/10.1103/PRXQuantum.1.020315)
25. M. Tsang, Cavity quantum electro-optics. *Phys. Rev. A* **81**, 063837 (2010). [doi:10.1103/PhysRevA.81.063837](https://doi.org/10.1103/PhysRevA.81.063837)
26. V. S. Ilchenko, A. A. Savchenkov, A. B. Matsko, L. Maleki, Whispering-gallery-mode electro-optic modulator and photonic microwave receiver. *J. Opt. Soc. Am. B* **20**, 333 (2003). [doi:10.1364/JOSAB.20.000333](https://doi.org/10.1364/JOSAB.20.000333)
27. L. Fan, C.-L. Zou, R. Cheng, X. Guo, X. Han, Z. Gong, S. Wang, H. X. Tang, Superconducting cavity electro-optics: A platform for coherent photon conversion between superconducting and photonic circuits. *Sci. Adv.* **4**, eaar4994 (2018). [doi:10.1126/sciadv.aar4994](https://doi.org/10.1126/sciadv.aar4994) [Medline](#)
28. L. Qiu, R. Sahu, W. Hease, G. Arnold, J. M. Fink, Coherent optical control of a superconducting microwave cavity via electro-optical dynamical back-action. [arXiv:2210.12443](https://arxiv.org/abs/2210.12443) [quant-ph] (2022).
29. See the supplementary materials.
30. A. Einstein, B. Podolsky, N. Rosen, Can quantum-mechanical description of physical reality be considered complete? *Phys. Rev.* **47**, 777–780 (1935). [doi:10.1103/PhysRev.47.777](https://doi.org/10.1103/PhysRev.47.777)
31. L.-M. Duan, G. Giedke, J. I. Cirac, P. Zoller, Inseparability criterion for continuous variable systems. *Phys. Rev. Lett.* **84**, 2722–2725 (2000). [doi:10.1103/PhysRevLett.84.2722](https://doi.org/10.1103/PhysRevLett.84.2722) [Medline](#)
32. R. Simon, Peres-horodecki separability criterion for continuous variable systems. *Phys. Rev. Lett.* **84**, 2726–2729 (2000). [doi:10.1103/PhysRevLett.84.2726](https://doi.org/10.1103/PhysRevLett.84.2726) [Medline](#)
33. Z. Y. Ou, S. F. Pereira, H. J. Kimble, K. C. Peng, Realization of the Einstein-Podolsky-Rosen paradox for continuous variables. *Phys. Rev. Lett.* **68**, 3663–3666 (1992). [doi:10.1103/PhysRevLett.68.3663](https://doi.org/10.1103/PhysRevLett.68.3663) [Medline](#)
34. H. Bernien, B. Hensen, W. Pfaff, G. Koolstra, M. S. Blok, L. Robledo, T. H. Taminiau, M. Markham, D. J. Twitchen, L. Childress, R. Hanson, Heralded entanglement between solid-state qubits separated by three metres. *Nature* **497**, 86–90 (2013). [doi:10.1038/nature12016](https://doi.org/10.1038/nature12016) [Medline](#)
35. S. Zippilli, G. D. Giuseppe, D. Vitali, Entanglement and squeezing of continuous-wave stationary light. *New J. Phys.* **17**, 043025 (2015). [doi:10.1088/1367-2630/17/4/043025](https://doi.org/10.1088/1367-2630/17/4/043025)
36. J. Agustí, Y. Minoguchi, J. M. Fink, P. Rabl, Long-distance distribution of qubit-qubit entanglement using Gaussian-correlated photonic beams. *Phys. Rev. A* **105**, 062454 (2022). [doi:10.1103/PhysRevA.105.062454](https://doi.org/10.1103/PhysRevA.105.062454)
37. S. Barzanjeh, S. Guha, C. Weedbrook, D. Vitali, J. H. Shapiro, S. Pirandola, Microwave quantum illumination. *Phys. Rev. Lett.* **114**, 080503 (2015). [doi:10.1103/PhysRevLett.114.080503](https://doi.org/10.1103/PhysRevLett.114.080503) [Medline](#)
38. C. Zhong, Z. Wang, C. Zou, M. Zhang, X. Han, W. Fu, M. Xu, S. Shankar, M. H. Devoret, H. X. Tang, L. Jiang, Proposal for heralded generation and detection of entangled

- microwave-optical-photon pairs. *Phys. Rev. Lett.* **124**, 010511 (2020).  
[doi:10.1103/PhysRevLett.124.010511](https://doi.org/10.1103/PhysRevLett.124.010511) [Medline](#)
39. S. Krastanov, H. Raniwala, J. Holzgrafe, K. Jacobs, M. Lončar, M. J. Reagor, D. R. Englund, Optically heralded entanglement of superconducting systems in quantum networks. *Phys. Rev. Lett.* **127**, 040503 (2021). [doi:10.1103/PhysRevLett.127.040503](https://doi.org/10.1103/PhysRevLett.127.040503) [Medline](#)
  40. S. Bravyi, O. Dial, J. M. Gambetta, D. Gil, Z. Nazario, The future of quantum computing with superconducting qubits. *J. Appl. Phys.* **132**, 160902 (2022). [doi:10.1063/5.0082975](https://doi.org/10.1063/5.0082975)
  41. J. Ang, G. Carini, Y. Chen, I. Chuang, M. A. DeMarco, S. E. Economou, A. Eickbusch, A. Faraon, K.-M. Fu, S. M. Girvin, M. Hatridge, A. Houck, P. Hilaire, K. Krsulich, A. Li, C. Liu, Y. Liu, M. Martonosi, D. C. McKay, J. Misewich, M. Ritter, R. J. Schoelkopf, S. A. Stein, S. Sussman, H. X. Tang, W. Tang, T. Tomesh, N. M. Tubman, C. Wang, N. Wiebe, Y.-X. Yao, D. C. Yost, Y. Zhou, Architectures for multinode superconducting quantum computers. [arXiv:2212.06167](https://arxiv.org/abs/2212.06167) [quant-ph] (2022).
  42. J. Knörzer, D. Malz, J. I. Cirac, Cross-platform verification in quantum networks. [arXiv:2212.07789](https://arxiv.org/abs/2212.07789) [quant-ph] (2022).
  43. R. Sahu, Data for: Entangling microwaves with light, Zenodo;  
<https://doi.org/10.5281/zenodo.7789418>.
  44. M. Tsang, Cavity quantum electro-optics. II. Input-output relations between traveling optical and microwave fields. *Phys. Rev. A* **84**, 043845 (2011).  
[doi:10.1103/PhysRevA.84.043845](https://doi.org/10.1103/PhysRevA.84.043845)
  45. A. Rueda, F. Sedlmeir, M. C. Collodo, U. Vogl, B. Stiller, G. Schunk, D. V. Strekalov, C. Marquardt, J. M. Fink, O. Painter, G. Leuchs, H. G. L. Schwefel, Efficient microwave to optical photon conversion: An electro-optical realization. *Optica* **3**, 597 (2016).  
[doi:10.1364/OPTICA.3.000597](https://doi.org/10.1364/OPTICA.3.000597)
  46. C. W. Gardiner, M. J. Collett, Input and output in damped quantum systems: Quantum stochastic differential equations and the master equation. *Phys. Rev. A Gen. Phys.* **31**, 3761–3774 (1985). [doi:10.1103/PhysRevA.31.3761](https://doi.org/10.1103/PhysRevA.31.3761) [Medline](#)
  47. S. L. Braunstein, P. van Loock, Quantum information with continuous variables. *Rev. Mod. Phys.* **77**, 513–577 (2005). [doi:10.1103/RevModPhys.77.513](https://doi.org/10.1103/RevModPhys.77.513)
  48. M. P. da Silva, D. Bozyigit, A. Wallraff, A. Blais, Schemes for the observation of photon correlation functions in circuit QED with linear detectors. *Phys. Rev. A* **82**, 043804 (2010). [doi:10.1103/PhysRevA.82.043804](https://doi.org/10.1103/PhysRevA.82.043804)
  49. D. Walls, G. Milburn, *Quantum Optics* (Springer, 1994).
  50. H. M. Wiseman, G. J. Milburn, *Quantum Measurement and Control* (Cambridge Univ. Press, 2009).
  51. C. M. Caves, Quantum limits on noise in linear amplifiers. *Phys. Rev. D Part. Fields* **26**, 1817–1839 (1982). [doi:10.1103/PhysRevD.26.1817](https://doi.org/10.1103/PhysRevD.26.1817)
  52. J. Wishart, The generalised product moment distribution in samples from a normal multivariate population. *Biometrika* **20A**, 32–52 (1928). [doi:10.1093/biomet/20A.1-2.32](https://doi.org/10.1093/biomet/20A.1-2.32)

- 53. S. Pirandola, G. Spedalieri, S. L. Braunstein, N. J. Cerf, S. Lloyd, Optimality of Gaussian discord. *Phys. Rev. Lett.* **113**, 140405 (2014). [doi:10.1103/PhysRevLett.113.140405](https://doi.org/10.1103/PhysRevLett.113.140405) [Medline](#)
- 54. G. Giedke, M. M. Wolf, O. Krüger, R. F. Werner, J. I. Cirac, Entanglement of formation for symmetric Gaussian states. *Phys. Rev. Lett.* **91**, 107901 (2003). [doi:10.1103/PhysRevLett.91.107901](https://doi.org/10.1103/PhysRevLett.91.107901) [Medline](#)